Phase change heat transfer in a vertical metal foam-phase change material thermal energy storage heat dissipator

Mehdi Ghalambaz[1*], S.A.M. Mehryan[2], Sayed Reza Ramezani[3], Ahmad Hajjar[4], Mohamad El Kadri[5], Mohamamd Saidul Islam[6], Obai Younis [7,8], Maryam Ghodrat[9]

[1] Institute of Research and Development, Duy Tan University, Da Nang 550000, Vietnam, Vietnam; mehdighalambaz@duytan.edu.vn; ghalambaz.mehdi@gmail.com
[2] Young Researchers and Elite Club, Yasooj Branch, Islamic Azad University, Yasooj, Iran.
[3] Department of Mechanical Engineering, K. N. Toosi University of Technology, Tehran, Iran
[4] ECAM Lyon, LabECAM, Université de Lyon, Lyon, France
[5] Centre Scientifique et Technique du Bâtiment, Champs-sur-Marne, France
[6] School of Mechanical and Mechatronic Engineering, Faculty of Engineering and Information Technology, University of Technology Sydney, Ultimo, NSW 2007, Australia
[7] Department of Mechanical Engineering, College of Engineering in Wadi Addwasir, Prince Sattam Bin Abdulaziz University, Al-Kharj 11942, Saudi Arabia.
[8] Department of Mechanical Engineering, Faculty of Engineering, University of Khartoum, Sudan
[9] School of Engineering and Information Technology, University of New South Wales Canberra, Canberra 2610 ACT, Australia. Email: m.ghodrat@unsw.edu.au
*Corresponding authors: Mehdi Ghalambaz (mehdighalambaz@duytan.edu.vn)

Abstract

A metallic foam heat dissipator for cooling electronic components was addressed. A heat dissipator is a partitioned aluminum container loaded along with aluminum metallic foam and saturated with paraffin wax. A heat flux at a surface contains a basic uniform flux and the step transient raise, which should be managed by a heat dissipator and a Phase Change Material (PCM). The regulating equations for a melting/solidification transfer of heat & momentum transport in a heat dissipator were instituted into a structure of partial differential equations. Then, the vital monitoring equations were converted into a general dimensionless type and solved by the Finite Element Method. A mesh adjustment technique & automated time-step control was employed to control the accuracy & convergence of the result automatically. An adaptation technique controls the mesh resolution at the melting/solidification interface. The dimensionless temperature of fusion is a vital factor in the control of the surface temperature and heat dissipator efficiency. Considering a fixed amount of material for walls, a heat dissipator with thick sidewalls and thin top and bottom walls results in slightly better thermal performance. Using a PCM heat sink could reduce the heated surface temperature by more than 175% during the pulse load.

Keywords: Phase change material heat dissipator; melting and solidification; metal foams; natural convection.

Nomenclature

Latin symbols	
A_{mush}	mushy constant ($kg.m^{-3}.s^{-1}$)
Bi	Biot number

C_p	heat capacity ($J.kg^{-1}.K^{-1}$)
Da	Darcy number
g	gravitational constant ($m.s^{-2}$)
h	convective heat transfer coefficient ($W.m^{-2}.K^{-1}$)
k	thermal conductivity ($W.m^{-1}.K^{-1}$)
MVF	normalized melted volume fraction
p	liquid pressure (Pa)
P	dimensionless liquid pressure
Pr	Prandtl number
q''	Heat flux ($W.m^{-2}$)
q''_0	heat flux at the heater element ($W.m^{-2}$)
Ra	Rayleigh number
s_w, s_b, s_t	Characteristics lengths
S_w, S_b, S_t	Geometrical non-dimensional parameters
Ste	Stefan number
t	time (s)
T	temperature field (K)
u	velocity in x-coordinate ($m.s^{-1}$)
U	dimensionless velocity in X-coordinate
v	velocity in y direction ($m.s^{-1}$)
V	dimensionless velocity in Y-coordinate
x	x-axis (m)
X	dimensionless X-coordinate

y	y-axis (m)
Y	dimensionless Y-coordinate

Greek symbols

α	heat diffusivity coefficient ($m^2.s^{-1}$)
β	coefficient of volumetric heat expansion (K^{-1})
γ	pulse power
Δt	pulse duration
ΔT	temperature scale (K)
$\Delta \tau$	dimensionless duration of the heat pulse
ε	porosity
η	the efficiency of composite-PCM heat dissipator
θ	dimensionless temperature
κ	permeability (m^2)
μ	dynamic viscosity (Pa.s)
ξ	the FEM's basis function
ρ	density ($kg.m^{-3}$)
τ	dimensionless time
ϕ	amount of molten PCM, melt (molten) volume fraction

Subscripts

∞	ambient
ave	average
b	bottom wall
f	phase change

fin	fin
l	PCM in a liquid state
m	effective of metal foam and PCM
s	PCM in a solid state
w	wall

Introduction

Phase Change Materials (PCM's) are considered by their high latent heat, which could absorb and discharge latent heat during melting and solidification processes. Therefore, PCMs are promising in several fields, such as energy storage, heat exchangers, building energy conservation, and electrical equipment. Nevertheless, PCMs low thermal conductivity is a disadvantage that sets a barrier to their use in industrial applications. The PCMs are commonly confined into an enclosure for preventing leaks & providing mechanical support. Hence, the advancement of the transfer of heat in enclosures is the crucial step in the enhancement of the transfer of heat of the PCMs.

Several techniques have been suggested to improve the transfer of heat into the cavity enclosures. A widely employed method consists of dispersing nanoparticles in the circulating fluid. For instance, Rachad et al. [1] researched natural convection in an inclined permeable area loaded with a Cu-water nanofluid. Sheikholeslami et al. [2] analyzed the magnetizable hybrid nanofluid of MWCNT-Fe_3O4/H_2O within a spherical void with two spherical heaters. Alsabery et al. [3] studied transient natural convection of an alumina-water nanofluid concentrated in a non-Darcy permeable medium. The convective heat transfer of nanofluids were also investigated in [4-7]. The results showed using nanoparticles can improve the heat transfer rate.

Moreover, the use of Nano-Encapsulated PCMs (NEPCMs) in forced convection and natural convection are also two methods for enhancing the PCMs thermal conductivity. Ho et al. [8] compared the forced convective cooling efficiency experimentally among two water-based suspensions in a spherical pipe warmed by continuous heat flux. The results indicate that for PCM suspension, the increases in suppressing maximum and surface-averaged wall temperatures were more than for nanofluid, but the local wall temperature suppression was lower. In the meantime, the effectiveness of Al2O3-water nanofluid in reducing local wall temperature decreased as the fluid moved downstream, whereas, for PCM suspension, a significant contribution by latent heat absorption due to melting progress occurred after an entry length from the heated section's inlet. The natural convective heat transfer of NEPCMs was also investigated in [9, 10], and the results showed that using NEPCM could effectively promote the natural convective heat transfer.

Another approach for transient heat transfer enhancement could be the use of the phase change material (PCMs). PCMs can help regulate the temperature or store energy with their signifinat latent heat of fusion. The phase change heat transfer in thermal energy storage units has been investigated in some recent publications. Mallya and Haussener [11] introduced a 2D model for energy storage and phase-change heat transfer simulation, considering the volumetric expansion and contraction effects, various temperature ranges, and multi-mode heat transfer. The authors studied the effect of natural convection on phase change. They tried to quantify the impact of geometrical parameters, thermophysical properties, and boundary conditions on the phase change process. A combination of the non-dimensional parameters such as the Nusselt, Rayleigh, Stefan, and Fourier numbers could link melt fraction and heat transfer rates. Gürtürk and Kok [12] explored using metallic fin inserts for the phase change and thermal energy storage. The outcomes revealed that the fin's surface area could assist heat transfer, but it could deteriorate the natural

convection circulation. The study of Ettouney et al. [13] shows that the impact of natural convection circulation on the phase change depends on the solidification or melting process.

Recent studies show the transfer of heat can further be improved by using conductive porous materials. Paknezhad et al. [14] employed an aluminum metal foam in a heatsink and investigated the impact of the tilted angle on the natural convection heat transfer circumstances along with & with no metallic foam. They found that the maximum cooling effectiveness of 17% is obtained at 90°C inclination angle when using the metal foam. Sivasankaran et al. [15] scrutinized a transfer of heat of a nanofluid in an inclined void loaded by a heat-producing permeable intermediate. The apertures were drenched with a nanofluid, which is water-based, containing Cu nanoparticles. The outcomes demonstrated that enhancing the permeability of the medium will improve the transfer of heat. Various aspects of flow and heat transfer in metal foams have been studied in other recent publications for internal heat generation and [16, 17] and magnetic field effects [18]. The flexible structures are also promising methods to improve heat transfer [19, 20]. For example, using a flexible fin could improve the heat transfer better than the rigid fin in an open-vented enclosure [20].

Recently, a new method was applied for enhancing the transfer of heat properties of the PCMs using metallic foams such as copper and aluminum foams, which have high thermal conductivity [21-23]. It consists of embedding PCMs in the foam's pores to produce PCM-metal foams with enhanced thermal conductivity. Several studies have addressed the efficiency of this technique. Zhang et al. [24] scrutinized mathematically & experimentally the melting transfer of heat attributes of copper/paraffin foam fusion PCM.

The application of non-homogeneous porous metal foams as thermal conductivity enhancers (TCEs) in energy storage systems and heat sinks containing phase change materials (PCMs) was

104 studied in [25]. The researchers used finite-volume discretization and the Darcy-Brinker-
105 Forchheimer model to investigate transient events inside PCM-based systems including TCEs with
106 gradient pore structure. The findings revealed that gradient porous TCEs may enhance the thermal
107 performance of PCMs by producing more uniform melting profiles and heat transfer distribution
108 across the whole system. In addition, the impacts of porosity factors on thermal sensitivity and
109 melting rate for chosen designs under varying heat load circumstances were investigated. Finally,
110 the thermal performance of uniform and gradient porous structures was evaluated for varied widths
111 and heights of the energy storage system. Overall, the results demonstrated that the application of
112 gradient porous TCEs may effectively enhance the thermal performance of PCM-based systems,
113 with the degree of improvement varies depending on the direction of the gradient foam with respect
114 to gravity and heat source position. Moreover, metal foam heat exchangers were investigated for
115 thermal enhancement of heat exchangers [26]. Mahjoob and Vafai [26] studied the impact of
116 microstructural metal foam features on heat exchanger performance, including porosity, pore and
117 fiber sizes, tortuosity, pore density, and relative density. The relevant relationships in the literature
118 for flow and thermal transfer in metal foam heat exchangers were classified and researched, and
119 three primary categories were developed. The use of a metal foam increased the performance factor
120 of foam-filled heat exchangers as compared to heat exchangers without foam.

121 Mancin et al. [27] researched a usage of copper foams for the enhancement of the change of
122 phase procedure with commissioning three distinct sections by 5, 10, & 40 PPI & continual
123 permeability equivalent to 0.95. PPI (Pores Per Inch) designates the number of pores in one linear
124 inch. Moreover, the impact of using metal foams in multiple PCM layer units [28], and air heat
125 exchangers [29, 30] have been investigated. All of these studies showed that embedding PCM

inside metal foams enhances PCMs rate of transfer of heat & thermal conductivity. Furthermore, the thermal discharging and charging rates were enhanced.

Zhen et al. [31] explored the melting conduct of paraffin in conjunction with & devoid of copper foam and studied an impact of a heating status on thermal operation capacity of copper/paraffin foam Composite-PCM (CPCM). They discovered that a melting time duration for a CPCM existed 20.5% smaller compared to absolute paraffin & that copper foam might drastically boost the consistency of PCMs temperature distribution. Al-Jethelah et al. [32] inspected a melting procedure of a nano-PCM into the square enclosure stuffed by the permeable intermediate theoretically. The outcomes revealed that a procedure of melting was enhanced with rising Darcy number (*Da*) & Rayleigh number (*Ra*). A high Rayleigh improves the effect of convection, most important for a rapid rate of melting. A large Darcy number improves the circulation of the melted PCM and boosts the melting rate.

In practical applications, such as charging and discharging processes in batteries, the thermal load is generally unsteady, contrary to the studies mentioned above. Khateeb et al. [33] examined a heat dissipation experimentally in the battery for four configurations: cooling by natural convection, the existence of Al foam as the matrix of transfer of heat, usage of PCM & mixture of PCM & Al foam. The results showed a reduction of 3-5°C in the temperature when using an Al foam-PCM as equated with absolute PCM.

Wang et al. [34] examined an Al/paraffin foam composite PCM experimentally. They found that employing Al/paraffin foam fused PCM had a standard impact on cooling during a discharge process by restricting a rise in the temperature of the battery of the Li-ion type. They also found that utilizing an aluminum foam might increase the speed of melting & enhance the PCMs temperature regularity. Li et al. [35] examined the impact of using copper foam-PCM composite

on the transfer of heat in 10 Ah batteries. The surface temperature decreased by 29% & 12% when equated to a temperature of a surface of convection of the air & the absolute PCM approach, correspondingly, at a 1 C rate of discharge. Ling et al. [36] experimentally analyzed the impact of utilizing heatsink with a phase change for the battery packs thermal supervision with the usage of CPCM (60 wt% RT44HC/expanded graphite (EG) composite & 60 wt% RT44HC/fumed silica composite). They found that the 60 wt% RT44HC/EG combined PCM could reduce a deviation of temperature between the cells. Ghalambaz & Zhang [37] modeled the cooling performance of a horizontal cylindrical enclosure filled with paraffin wax PCM around a cylindrical battery. The PCM was embedded in Nickel-metal foam and acted as a thermal management structure for damping thermal transient loads of the battery. An external flow cooled an exterior surface of a cavity while the interior surface of a cavity was a battery's surface by the transient heat-flux. The writers discovered that the existence of PCM-metallic foam in an enclosure could effectively manage the battery's temperature during the transient thermal loads of the charging or discharging process. Using PCM-metal foam was more beneficial when the external cooling flow was weak.

The literature review showed that the heat transfer capability of PCM heatsinks could be improved by using metal foam. A heat dissipator with a thermal storage capability could effectively dampen transient heat loads in electronic components. The study by Ghalambaz & Zhang [37] showed a single horizontally mounted dissipator could dampen some of the transient loads exerted on a heater. However, there are many application cases where the dissipator should be mounted vertically on the heater or the dissipator is made of several PCM blocks. Thus, the geometrical structure of a PCM-heat dissipator is an important design issue to not only keep the electronic component cool during steady-state operation but also dampen the transient heat loads

on demand. The present study aims to address the cooling behavior of a vertically mounted heat dissipator over a heated surface for the first time.

2. Mathematical model:

As displayed in Fig. 1 (a), the heatsink made of aluminum is loaded with aluminum metallic foam by the porosity of ε and permeability of κ. Inside, a permeable intermediate is concentrated by paraffin wax PCM along with a temperature of fusion of T_f. A time-dependent heat source was located beneath the heatsink, which produces a base power of $q_0^{''}$. The power could be raised to $(1+\gamma)q_0^{''}$ through the time period of p, i.e. (t_1-t_0), and later decreases to a base heat-flux $q_0^{''}$ for a sufficiently long time. It is worth noting that γ is known as heating pulse power. The apex of the heatsink is reliant to a cooling convective transfer flow by a uniform temperature (T_∞) where T_∞°<°T_f, and a convective power of h_∞.

Aluminum foams have a few advantages over copper heatsinks. Aluminum foams are lighter than copper foams, which might be advantageous in situations where weight is an issue. Moreover, aluminum foams are often less costly than copper foams, which might make them a more cost-effective alternative. Enhanced thermal conductivity is an additional benefit of aluminum heatsinks. Copper has slightly better thermal conductivity than aluminum, but aluminum foams are still able to efficiently dissipate heat owing to their greater surface area-to-volume ratio. Copper foams could be simpler to fabricate than aluminum foams. Aluminum is more pliable than copper, allowing for the foam to be shaped and formed more easily and efficiently. This may lead to a faster and more efficient manufacturing process. Copper foams may have certain benefits in terms of thermal conductivity, but aluminum foams are a lightweight, cost-effective, and efficient heat dissipation solution for many applications. Thus, aluminum foams were adopted over copper foams in the present study. Moreover, PCMs derived from paraffin possess a high latent heat of

fusion, a low melting point, are non-toxic and are sustainable. They can successfully cool electronic components that generate heat at low temperatures and are economical, making them an appealing alternative for cooling electronic components.

The heatsink will be mounted vertically on a hot surface so that gravity is acting along the hot surface, so revealed in Fig. 1(a). At an initial time, PCM is at an actual constant temperature of T_∞. After that, a heat-flux rises to a base power of $q_0^{"}$ for a suitably long time while waiting for a heatsink to attain its stable-state condition. Later unexpectedly, a heat-flux rises up to an elevated heat-flux $(1+\gamma)q_0^{"}$ through the time period of p. After the time interval of p the heat flux reduces back up to a base heat-flux. A profile of heat-flux is illustrated in Fig. 1(c). As seen, all of the cells are similar. One of the cells is revealed in Fig. 1(a) by the green dash-line. Fig. 1(b) shows this cell in more detail. Since the cells are identical, just a single cell is patterned here and analyzed. Subsequently, the outcomes could be transformed into a unit length of a heat dissipator. The attributes of PCM (paraffin wax) & metal foam are provided in Table 1. The thermophysical properties were considered temperature independent except the change liquid PCM volume which was modeled using the Boussinesq approximation. The temperature difference between the metal foam and PCM inside the pores was also ignored leading to a thermal equilibrium model of metal foam PCM. During the melting process, temperature discrepancies may arise between the metal foam and PCM in places adjacent to the heat source or solid/liquid border. This may be approximated using a local thermal non-equilibrium (LTNE) technique, however empirical studies indicate that the LTNE condition is only important at the start of the melting process [38]. Experimental and computational investigations demonstrate that the LTNE condition diminishes as the melting process advances [39-41]. As a result, for the sake of simplicity, the local thermal

equilibrium (LTE) model is often utilized for thermal energy storage applications, as well as in this work.

Taking into account the presumptions stated overhead, a set of regulating equations for a molten PCM flow & transfer of heat into a free layer & permeable intermediate layer was recorded as follows [42-44]:

$$\frac{\partial u}{\partial x}+\frac{\partial v}{\partial y}=0 \tag{1}$$

$$\frac{\rho_l}{\varepsilon}\frac{\partial u}{\partial t}+\frac{\rho_l}{\varepsilon^2}\left(u\frac{\partial u}{\partial x}+v\frac{\partial u}{\partial y}\right)=-\frac{\partial p}{\partial x}+\frac{\mu_l}{\varepsilon}\left(\frac{\partial^2 u}{\partial x^2}+\frac{\partial^2 u}{\partial y^2}\right)-\frac{\mu_l}{\kappa}u-s(T)u \tag{2}$$

$$\frac{\rho_l}{\varepsilon}\frac{\partial v}{\partial t}+\frac{\rho_l}{\varepsilon^2}\left(u\frac{\partial v}{\partial x}+v\frac{\partial v}{\partial y}\right)=-\frac{\partial p}{\partial y}+\frac{\mu_l}{\varepsilon}\left(\frac{\partial^2 v}{\partial x^2}+\frac{\partial^2 v}{\partial y^2}\right)-\frac{\mu_l}{\kappa}v-s(T)v+\rho_l g\beta_l\left(T-T_f\right) \tag{3}$$

Energy conservation in composite metal foam:

$$(\rho C_p)_m\frac{\partial T}{\partial t}+(\rho C_p)_l\left(u\frac{\partial T}{\partial x}+v\frac{\partial T}{\partial y}\right)=k_m\left(\frac{\partial^2 T}{\partial x^2}+\frac{\partial^2 T}{\partial y^2}\right)-\rho_l h_{sf}\frac{\partial\phi(T)}{\partial t} \tag{4}$$

in which

$$(\rho C_p)_m=\phi(\rho C_p)_{m,l}+(1-\phi)(\rho C_p)_{m,s}\;\left|\begin{array}{l}(\rho C_p)_{m,l}=(1-\varepsilon)(\rho C_p)_p+\varepsilon(\rho C_p)_l\\(\rho C_p)_{m,s}=(1-\varepsilon)(\rho C_p)_p+\varepsilon(\rho C_p)_s\end{array}\right. \tag{5}$$

The variables u and v of the above-expressed equations are velocity variables along with x and y coordinates. p is the pressure variable, $S°(T)$ is the momentum source, T is the temperature variable, ϕ is the melted fraction variable, and t is the time. Here, ρ is density, ε is the porosity, μ is dynamic viscosity. The symbols β, C_p, and k are the thermal-volume expansion coefficient, sensible heat capacity, and thermal conductivity. The latent heat capacity of the PCM was denoted by h_{sf}. The subscripts of l and s identify the PCM's liquid and solid states. Besides, m denotes the effective properties of the porous medium.

As given in momentum and energy controlling equations, the melting process is modelled via the momentum and energy sink terms, i.e., s (T) and $-\rho_l h_{sf}\ \partial\phi(T)/\partial t$. In this model, the domain is divided into three zones, fully melted, partially melted, and fully solid zones, controlled by $s°(T)$ sink terms. It is worth mentioning that the partially-melted zone is known as the mushy zone. $s°(T)$ term controls the velocity of the zones according to Eqs. (6) and (7). In this relation, e is a small number utilized to avoid division by zero. Also, A_{mush} is a constant with a large value, which as adopted as 1×10^6 kg/(m^{3}s). As expressed in Eq. (6) and (7), when the domain temperature is less than the melting temperature, i.e., $\phi(T)=0$, $s°(T)$ tends towards a large value resulting in infinity resistance against the PCM flow. Consequently, when the liquid fraction, i.e., $\phi(T)$, reaches 1, the cell only contains liquid. For the other state given for $\phi(T)$, a cell is partially occupied by both solid and liquid phases of PCM.

$$s(T)=A_{mush}\frac{\left(1-\phi(T)\right)^2}{\phi(T)^3+e} \tag{6}$$

$$\phi(T)=\begin{cases}0 & T<T_f\\ \dfrac{T-T_f}{\delta T} & T_f<T<T_f+\delta T\\ 1 & T>T_f+\delta T\end{cases} \tag{7}$$

The following model was used to evaluate the effective thermal conductivity of composite metal foam and PCM [45]:

$$k_m=\frac{\left[k_l+\pi\left(\sqrt{\frac{1-\varepsilon}{3\pi}}-\frac{1-\varepsilon}{3\pi}\right)\left(k_p-k_l\right)\right]\left[k_l+\frac{1-\varepsilon}{3}\left(k_p-k_l\right)\right]}{k_l+\left[\frac{4}{3}\sqrt{\frac{1-\varepsilon}{3\pi}}\left(1-\varepsilon\right)+\pi\sqrt{\frac{1-\varepsilon}{3\pi}}-\left(1-\varepsilon\right)\right]\left(k_p-k_l\right)} \tag{8}$$

where subscript *p* refers to the solid matrix.

Finally, the subsequent equation can be expressed for a solid impermeable wall:

$$\left(\rho C_p\right)_w \frac{\partial T_w}{\partial t} = k_w \left(\frac{\partial^2 T_w}{\partial x^2} + \frac{\partial^2 T_w}{\partial y^2} \right) \tag{9}$$

The periodic thermal boundary conditions are employed for the sidewalls:

$$\frac{\partial T_w\left(0,y\right)}{\partial y} = \frac{\partial T_w\left(l_h,y\right)}{\partial y} \quad and \quad T_w\left(0,x\right) = T_w\left(l_h,x\right) \tag{10-a}$$

The top wall was cooled convectively:

$$-k_w \frac{\partial T_w\left(x,l_w\right)}{\partial x} = h_\infty \left(T_w - T_\infty\right) \tag{10-b}$$

The prescribed heat flux bottom is applied at the bottom wall:

$$-k_w \frac{\partial T_w\left(x,0\right)}{\partial x} = q''\left(t\right)$$
$$q''\left(t\right) = \begin{cases} \left(1+\gamma\right) q_0'' & t_0 < t < t_1 \\ q_0'' & t < t_0 \,,\, t > t_1 \end{cases} \tag{10-c}$$

in which t_0°=100*s*. The steady-state solution was considered for the field variables at t=0s. The continuity of temperature and heat flux were applied at the conjugate surfaces [46]:

$$T_w\big|_{wall} = T\big|_{porous} \,,\; k_w \left.\frac{\partial T_w}{\partial n}\right|_{wall} = k_m \left.\frac{\partial T}{\partial n}\right|_{porous} \tag{10-d}$$

In above, *n* represents a normal direction to a surface. The walls and a melting interface are counted as impervious & no-slip employed for fluid flow. The zero-pressure relative pressure as a reference point was presumed at the bottom side left corner. It is suitable to express Eqs. (1)– (10) into a dimensionless format by invoking scaling variable and constant parameters.

variable parameters

$$X=\frac{x}{H},\ Y=\frac{y}{H},\ U=\frac{uH}{\alpha_{m,l}},\ V=\frac{vH}{\alpha_{m,l}},\ \theta=\frac{T-T_{\infty}}{\Delta T},\ S(\theta)=\frac{s(T)H^2}{\rho_l\alpha_{m,l}}$$
$$P=\frac{pH^2}{\rho\alpha_{m,l}^2},\ \tau=\frac{t\alpha_{m,l}}{H^2} \quad (11\text{-a})$$

constant parameters

$$\alpha_{m,l}=\frac{k_{m,l}}{\left(\rho c_p\right)_{m,l}},\ Pr=\frac{\mu_l}{\rho_l\alpha_{m,l}},\ Ra=\frac{g\rho_l\beta_l\Delta TH^3}{\alpha_{m,l}},\ Ste=\frac{\Delta T\left(\rho C_p\right)_{m,l}}{h_{sf}\rho_l},\ Da=\frac{\kappa}{H^2} \quad (11\text{-b})$$

where $H = l_h$ is a characteristic length, and *Pr* and *Ra* are the Prandtl and Rayleigh numbers. *Ste* and *Da* are Stefan and Darcy numbers. Here, ΔT is introduced based upon a temperature scaling specified a $\Delta T = q_0'' H / k_{m,l}$ where $k_{m,l}$ is the effective thermal conductivity of a liquid PCM concentrated metallic foam. Eq. (11) is plugged into dimensional governing equations, a scaled form of the equations was achieved as follows:

Momentum equation in *x*- and y- directions

$$\frac{1}{\varepsilon}\frac{\partial U}{\partial\tau}+\frac{1}{\varepsilon^2}\left(U\frac{\partial U}{\partial X}+V\frac{\partial U}{\partial Y}\right)=-\frac{\partial P}{\partial Y}+\frac{Pr}{\varepsilon}\left(\frac{\partial^2 U}{\partial X^2}+\frac{\partial^2 U}{\partial Y^2}\right)-\frac{Pr}{Da}U-S(\theta)U \quad (12)$$

$$\frac{1}{\varepsilon}\frac{\partial V}{\partial\tau}+\frac{1}{\varepsilon^2}\left(U\frac{\partial V}{\partial X}+V\frac{\partial V}{\partial Y}\right)=-\frac{\partial P}{\partial X}+\frac{Pr}{\varepsilon}\left(\frac{\partial^2 V}{\partial X^2}+\frac{\partial^2 V}{\partial Y^2}\right)-\frac{Pr}{Da}V-S(\theta)V+PrRa\theta \quad (13)$$

Thermal equation for composite PCM:

$$\left(\frac{(\rho C_p)_m}{(\rho C_p)_{m,l}}\right)\left(\frac{\partial\theta}{\partial\tau}\right)+\left(\frac{(\rho C_p)_l}{(\rho C_p)_{m,l}}\right)\left(U\frac{\partial\theta}{\partial X}+V\frac{\partial\theta}{\partial Y}\right)=\left(\frac{k_m}{k_{m,l}}\right)\left(\frac{\partial^2\theta}{\partial X^2}+\frac{\partial^2\theta}{\partial Y^2}\right)-\left(\frac{\varepsilon}{Ste}\right)\frac{\partial\phi(\theta)}{\partial\tau} \quad (14)$$

Thermal equation for the solid conjugate walls:

$$\left(\frac{\left(\rho C_p\right)_w}{\left(\rho C_p\right)_{m,l}}\right)\frac{\partial\theta_w}{\partial\tau}=\left(\frac{k_w}{k_{m,l}}\right)\left(\frac{\partial^2\theta_w}{\partial X^2}+\frac{\partial^2\theta_w}{\partial Y^2}\right) \quad (15)$$

In addition, using the characteristic length, i.e., *H*, the geometrical non-dimensional parameters are

$$S_w = \frac{s_w}{H}, S_b = \frac{s_b}{H}, S_t = \frac{s_t}{H}, L_h = \frac{l_h}{H} \tag{16}$$

In the above-expressed equations, the ratios of thermophysical properties appeared since we performed the non-depersonalization process based on the liquid properties. Moreover, the non-dimensional equations deal with less independent parameters. For example, the size of the heat dissipator, temperature difference, and gravity parameters are grouped in the Rayleigh number. The imposed boundary conditions in the dimensionless coordinates are

$$\frac{\partial \theta_w(0,X)}{\partial Y} = \frac{\partial \theta_w(L_h,X)}{\partial Y} \quad and \quad \theta_w(0,X) = \theta_w(L_h,X) \tag{17-a}$$

$$\left(\frac{k_w}{k_{m,l}}\right)\frac{\partial \theta_w(X,1)}{\partial X} = Bi\theta_w \mid Bi = \frac{h_\infty H}{k_{m,l}} \tag{17-b}$$

$$\left(\frac{k_w}{k_{m,l}}\right)\frac{\partial \theta_w(X,0)}{\partial X} = \delta(\tau) \mid \delta(\tau) = \begin{cases} 1+\gamma & \tau_0 < \tau < \tau_1 \\ 1 & \tau < \tau_0, \tau > \tau_1 \end{cases}, \tau_1 = \frac{t_1 \alpha_{m,l}}{H^2} \tag{17-c}$$

$$\theta_w\big|_{wall} = \theta_l\big|_{porous}, \quad \frac{k_w}{k_{m,l}}\frac{\partial \theta_w}{\partial N}\bigg|_{wall} = \frac{k_m}{k_{m,l}}\frac{\partial \theta}{\partial N}\bigg|_{porous} \tag{17-d}$$

The zero non-dimensional pressure relative pressure (P=0) was presumed at the bottom side left corner as a reference point. It should be noted that x is applied in vertical direction normal to the heated surface. The non-dimensional thermophysical characteristics could be reviewed as:

$$\begin{aligned} &\frac{k_{m,s}}{k_{m,l}} = \frac{(1-\varepsilon)k_p + \varepsilon k_s}{(1-\varepsilon)k_p + \varepsilon k_l}, \quad \frac{k_w}{k_{m,l}} = \frac{k_w}{(1-\varepsilon)k_p + \varepsilon k_l} \\ &\frac{(\rho C_p)_w}{(\rho C_p)_{m,l}} = \frac{(\rho C_p)_w}{(1-\varepsilon)(\rho C_p)_p + \varepsilon(\rho C_p)_l}, \quad \frac{(\rho C_p)_{m,s}}{(\rho C_p)_{m,l}} = \frac{(1-\varepsilon)(\rho C_p)_p + \varepsilon(\rho C_p)_s}{(1-\varepsilon)(\rho C_p)_p + \varepsilon(\rho C_p)_l} \end{aligned} \tag{18}$$

The relation describing the phase field variable in the dimensionless coordinates are:

$$\phi(\theta)=\begin{cases}0 & \theta<\theta_f \\ \dfrac{\theta-\theta_f}{\delta\theta} & \theta_f<\theta<\theta_f+\dfrac{\delta T}{\Delta T} \\ 1 & \theta>\theta_f+\dfrac{\delta T}{\Delta T}\end{cases} \tag{19}$$

An important factor of the current research is a dimensionless temperature of a bottom wall, where defined as:

$$\theta_b=\frac{T_b-T_\infty}{\Delta T} \tag{20}$$

The local wall temperature, i.e., θ_b, indicates a local wall temperature of an element. Accordingly, the average bottom wall temperature can be evaluated as:

$$\theta_{b,ave}=\frac{\int_0^{L_h}\theta_b\,dL}{L_h} \tag{21}$$

Here, the melting volume fraction is calculated as:

$$MVF=\frac{\int_A \varepsilon\phi dA}{\int_A \varepsilon dA} \tag{22}$$

The heat dissipator effectiveness, η, could be assessed by equating an element temperature in the presence of heat dissipator ($\theta_{b,ave}$) with a case without the presence of the heat dissipator ($\theta_{b,woh}$) in which the element is subject to direct cooling by the forced convection. In a situation without heat dissipator, the energy equilibrium at an element surface could be introduced as:

$$q''(t)\times H = H\times h_\infty\left(T_{b,woh}-T_\infty\right) \tag{23}$$

Subscript *woh* refers to the case without the heat dissipator structure of the heater element. The dimensionless form of the above equation could be obtained as:

316 $$\theta_{b,woh}=\frac{1+\gamma(\tau)}{Bi}\ |\ \gamma(\tau)=\begin{cases}\gamma & \tau_0<\tau<\tau_1\\ 0 & \tau<\tau_0\,,\tau>\tau_1\end{cases}\ and\ Bi=\frac{h_\infty H}{k_{m,l}} \quad (24)$$

317 *Bi* of the above equation is Biot number and $\tau_0=0.02098$. Eventually, the efficiency of the
318 composite cell defined based on the ratio of element temperature at the presence of heat dissipator
319 to that without the presence of heat dissipator could be concluded as:

320 $$\eta=\frac{\theta_{b,ave}}{\theta_{b,woh}}=\frac{Bi\ \theta_{b,ave}}{1+\gamma(\tau)} \quad (25)$$

321 Also, it is worth noting that the average Nusselt number on the hot surface can be expressed as the
322 following [3]:

323 $$Nu=\frac{k_m}{k_{m,l}}\int_0^{l_w}\left.\frac{\partial\theta}{\partial X}\right|_{X=0} dy \quad (26)$$

324

3. Numerical approach

3.1. Finite Element Method (FEM)

The FEM, founded on a weighted residual method, is applied to integrate the model's equations. Herein, the conservation of mas acts as a constraint governing a pressure supply. A basis set $\{\xi_k\}_{k=1}^{N}$ is defined to expand the unknown variables including U, V, θ, and θ_w as follows:

$$U \approx \sum_{k=1}^{N}\left(U_k \xi_k\left(X, Y\right)\right), V \approx \sum_{k=1}^{N}\left(V_k \xi_k\left(X, Y\right)\right), \theta \approx \sum_{k=1}^{N}\left(\theta_k \xi_k\left(X, Y\right)\right), \theta_w \approx \sum_{k=1}^{N}\left(\theta_{w_k} \xi_k\left(X, Y\right)\right) \quad (27)$$

Since the basis function which expands the variables is alike for all the variables, the overall number of nodes and the number of variables is the same, i.e., N=4. The nonlinear residuals relations associated with the equations are obtained. The integration of weak equations over the domain elements resulted in the matrix of coefficient, which was solved by the Newton method for field variables in a coupled way approach.

The approach of three points Gaussian is employed to assess the integrations. In addition, nonlinear residual equations have been resolved by utilizing a Newton-Raphson method. The stream function ψ is applied to visualize a flow field of a melted PCM inside the porous medium:

$$\frac{\partial^2 \psi}{\partial X^2} + \frac{\partial^2 \psi}{\partial Y^2} = \frac{\partial U}{\partial Y} - \frac{\partial V}{\partial X} \quad (28)$$

The values of ψ on the walls are taken zero. Stream function can be approximated using the basis set defined above, i.e. $\{\xi_k\}_{k=1}^{N}$,

$$\psi \approx \sum_{k=1}^{N} \psi_k \xi_k\left(X, Y\right) \quad (29)$$

The nonlinear residual equation obtained by employing the Galerkin finite element approach for stream functions is

$$R_i^3 \approx \sum_{k=1}^{N} \psi_k \int \left[\frac{\partial \xi_i}{\partial X}\frac{\partial \xi_k}{\partial X} + \frac{\partial \xi_i}{\partial Y}\frac{\partial \xi_k}{\partial Y} \right] dX dY - \int \frac{\partial}{\partial X}\left(\sum_{k=1}^{N} V_k \xi_k \right) \xi_i dX dY + \int \frac{\partial}{\partial Y}\left(\sum_{k=1}^{N} U_k \xi_k \right) \xi_i dX dY \quad (30)$$

It is worth noting that the PARDISO solver was chosen with a relative tolerance of 5×10^{-4} for all the variables. The time step is automatically selected by utilizing the Backward Differentiation Formula (BDF). The algorithm of the numerical method is shown in the chart represented in Fig. 2.

3.2. Grid independency examination

It is believed that a heat dissipator generates a heat-flux at the bottom surface with an extreme amount of γ=3 for the period of p=1100 s discharge load. The discharging begins at t_0=100 s & goes on up to t_1=1200s. The non-dimensional factors equivalent to the mentioned case are calculated as: $Ra = 3.7315\times10^7$, $Da = 1.2\times10^{-5}$, $Pr = 1.17155$, $Bi = 2.2989$, $\varepsilon = 0.9486$, $\theta_f = 0.62637$, $\gamma = 3$, $k_w/k_{m,l} = 46.531$, $(\rho C_p)_w/(\rho C_p)_{m,l} = 1.0225$, $(\rho C_p)_{m,s}/(\rho C_p)_{m,l} = 1$, $\tau_0 = 0.02098$, and $p = 0.23084$. The outcomes of the current research would be described for these parameters; otherwise, the changes would be specified. Using triangular cells could lead to more flexibility over complex domains while quadrilateral cells could provide higher accuracy and lower computational costs. Here, our code was well suited to work with triangular cells, and hence, triangular cells were adopted for the discretization of the domain. Moreover, a mesh adaptation was applied at the melting interface to better capture the phase change and field variables at the phase change interface. The adaptation was only compatible with the triangular cells. The mesh adaptation was updated every 120 seconds and was performed on the domain area with $0.05 < \phi < 0.95$.

Moreover, a backward differentiation formula was employed to adjust time-steps and the accuracy & convergence of the simulations automatically

The details of the mesh and results are reported in Figs. 3, 4, and Table 2. Case IV was selected for the remainder of the computation as a reasonable compromise between computational expense and computational precision. Fig. 3(a) shows a sharp raise of base temperature at the initial times up to a pick at τ=0.5 due to boosted heat flux. Then a smooth drop in temperature due to the cooling of the top surface can be observed. Fig. 3(b) also shows a pick MVF of about 0.7 at τ=0.5. However, after this time the melting volume fraction drops smoothly since the cooling power of the top surface subject to the convection heat transfer is more power full than the initial state of the heater. Maximum efficiency can be seen at initial times (τ<0.3) where the MVF is quite low and the PCM heatsink is cool.

3.3. Validations and verifications

The correctness of the applied numerical approach is verified and validated through comparisons between the simulation results and those of experimental & mathematical valid workings presented in the literature [47-55]. In Fig. 5, the advancement of a melting front related to the PCM inside a clear enclosure, which was presented in the literature review [54] is chosen for the evaluation. The PCM occupying the enclosure is Octadecane with Pr = 50 and Ste = 0.1. There are some differences between the evaluated melting interfaces by various numerical approaches. The reason could be the difference between the applied mushy parameters, numerical methods, and various mesh resolutions at the melting interface. However, the trend of the results for all investigations is following a similar pattern. In order to further investigate the melting phenomena several more comparisons were performed.

As depicted in Fig. 6, the experimental results exhibited by Kumar et al. [53] and the mathematical outcomes of a current study are compared for several melting times. The working phase change material in the investigated stainless cubic was lead. A heater imposed an iso heat-flux on the right wall of a cubic, whereas the other walls were perfectly insulated. The values of non-dimensional parameters for this comparison are $Ra = 1.4\times10^{7}$, $Pr = 0.0236$, and $Ste = 0.4$. It is worth noting that the *Ra* and *Ste* defined in the research of Kumar et al. [53] are different from the *Ra* and *Ste* presented in the current work. As seen, the results for both studies are in good agreement and the simulation interface follows the measured melting interface well.

In another validation (presented in Fig. 7), the melting fields obtained from the present numerical solution are compared with the experimental and numerical fields presented in Kamkari and Amlashi [55]. Lauric acid as PCM filled a container 12 cm depth, 5 cm wide, and 12 cm height. The right side of the container was kept at a high constant of 70 °C, and the other walls were isolated. *Ra*, *Pr*, and Ste as the non-dimensional governing parameters are 8.3×10^{8}, 100.7, and 0.52, respectively. The present investigation demonstrated an excellent match between the simulated melted area and the numerical simulations, providing strong support for the existing computational model's dependability and precision. The correlation between simulation results and the calculated molten zone demonstrates that the model can properly anticipate the thermal behavior of the phase transition material. These results support the use of the existing model for studying and constructing phase transition material-based. The excellent agreement between the simulated and computed melted area offers confidence in the model's capacity to properly represent the complicated heat transport and phase change processes that occur inside the PCM heatsink.

Considering steady-state conditions (after a long time) and neglecting the conjugate effect, the verification was performed with a conventional saturated porous medium, which was examined by numerous researchers. In this case, the evaluation of the calculated values of the average Nusselt number for Rayleigh number is reported in Table 3 [47-52].

In [31], the melting phase change heat transfer in a cavity filled with copper metal foam and saturated with Paraffin-wax was studied. The cavity was insulated from the sidewalls and was dependent on the uniform heat-flux of 1150 W/m^2 at a top. The numerical outcomes of the current research are equated with the findings of [31]. The following thermophysical properties & boundary conditions were adopted: $k_{m,l}$ = 5.0 W/mK [56], $k_{m,s} = k_{m,l}$, ρ_p = 8900 kg/m^3, C_p = 386 J/kg.K, $\kappa = 2.7\times10^{-7}$m^2 (based on the range of literature data in [57] and [58]), q'' = 1150 W/m^2, the heat lost from each of the sidewalls and bottom walls q''_{loss} = -17.5w/m^2, cavity size H = 0.1 m, bulk porosity ε = 0.975 (the surface porosity ε = 0.95). The corresponding non-dimensional parameters are $Ra = 1.3161\times10^7$, $Da = 2.7\times10^{-5}$, Pr = 1.5135, and Ste = 0.35516. The non-dimensional heat-flux at the top is one & the heat loss at each of the sidewalls and bottom wall is 0.0152 (1.52%). The temperature scale was calculated as ΔT = 22.977 °C. Fig. 8 shows the evaluation of the outcomes of [31] & the numerical findings of the current research. As Per observation, the outcomes are in an exceptional accord showing the capability of the present model and simulations for capturing phase change heat transfer in metal foams.

3.4. Non-dimensional parameters

In directive to achieve a feasible range of the dimensionless parameters, the subsequent default thermophysical properties, temperatures, and geometrical specifications were adopted: Aluminum metal foam with the following properties: 10 PPI with ε = 0.9486, $\kappa = 1.2\times10^{-7}$ m^2 [58] The effective thermal conductivity of a permeable medium & PCM is evaluated using Eq. (6) as:

k_m = 4.35 W/m.K. The geometrical dimensions of the model are l_w = l_h=0.1 m and s_w = s_t =s_b = 0.025×l_w. The fusion temperature of the PCM T_f is 50 °C. The ambient air temperature and convection heat transfer coefficient are T_∞ = 40 °C and h_∞ = 100 W/m^{2}K, respectively. The base heat flux $q_0^{"}$ is 2500 W/m^2. The pulse power and duration are γ = 1 and Δt = 1200 s, respectively. The corresponding non-dimensional parameters are: *Ste* = 0.88837, *Da* = 1.2×10^{-5}, *Pr* = 1.7155, *Bi* = 2.23, *Ra* = 3.7315×10^7. The non-dimensional pulse duration is evaluated as $\Delta\tau$ = 0.23084, and the non-dimensional fusion temperature is evaluated as θ_f = 0.626. A time scale parameter is also calculated as ΔT = 57.747 °C.

4. Results and discussions

The non-dimensional metal fin surface area can be evaluated as A_{fin}=(S_b+S_t)×(1+2×S_w)+2×S_w=0.32. In the present study, the thicknesses of S_b, S_t, and S_w will be changed in a way that a total surface area of a fin remains constant as A_{fin}=10.25% total surface area of a fin.

The type and attributes of a metallic foam and PCM are fixed in the present study. The geometrical parameters of interest are the thickness of the solid walls by considering the introduced constraint for A_{fin}. The effect of pulse power γ, pulse duration $\Delta\tau$, as well as *Bi* on the average temperature profiles of an element is of interest. Melting and recharging times of the heat dissipator are also of interest.

Fig. 9 depicts the streamlines & the isothermal contours in an enclosure at various instants.
It should be noted that zones occupied by streamlines correspond to the liquid phase, i.e., where PCM has melted. Initially, the PCM is melting near the hot lower wall. Initially (Fig. 9(a)), the isotherms are almost stratified along y direction (note that the y direction is in the horizontal direction), indicating a conduction-dominated heat transfer. The streamlines form a small

recirculation zone as convection is starting to develop, so the hot liquid goes to the left and the colder one to the right; the gravity is assumed to be acting in a y-direction. In an early stage of a heat pulse (Fig. 9(b)), a high-temperature gradient appears near the lower wall, and the convection begins to dominate after the activation of the hot pulse. The recirculation zone increases in size as PCM melting is intensified. The hot moving fluid near the lower wall accelerates on the left part of the solid zone, resulting in an inclined melting interface. Soon when a heat pulse is turned off (Fig. 9(c)), the overall temperature of a cavity rises, the melting of PCM reaches its maximum. Liquid PCM covers most of the cavity, except a small region located in the upper right region. After that, (Fig. 9(d) and (e)), the temperature of the cavity starts to decrease, and the melted zone shrinks, and finally (Fig. 9(f)), the liquid PCM only occupies the lower part half of the cavity.

Fig. 10 illustrates the streamlines & the temperature distribution for various fusion temperatures θ_f at τ=0.3158. As discussed in Fig. 9, this corresponds to the instant soon later a heat pulse is turned off. It is clear that the melting is maximized for θ_f=0.539 compared to the other values. Increasing θ_f above that value reduces the melting zone of the PCM, which is at its lowest for θ_f=0.696. In fact, the PCM undergoes melting when the temperature of a surrounding is greater than θ_f. Consequently, for the low-value θ_f, all the PCM in the cavity melts. On the other hand, when θ_f is increased above 0.6; for example, the PCM near the upper wall does not melt as the temperature in that cold region remains below its fusion temperature. Raising θ_f, thus, increases the zone in which the temperature is lower than a PCM fusion temperature and diminishes melting.

The streamlines and the melt volume fraction contours in the cavity are illustrated in Fig. 11 at different instants. The MVF contours indicate that a melting gradient occurs in the melting interface. In fact, the melting interface is not a single line separating liquid and solid PCM. It is rather a region between the two phases, having a spectrum ranging from MVF=1 in a liquid phase

to 0 in a solid phase. Between these two limits, PCM partially undergoes a phase change when a temperature is close to its fusion temperature. Considering these images and the model of Fig. 1(b), gravity acts from top to bottom while the left wall is heated and the right wall is cooled. The top and bottom walls are also under periodical heating/cooling conditions due to the periodic nature of the whole heatsink model. Thus, as seen, the convection heat transfer circulations commence next to the right wall and extend toward the left wall. Moreover, the advancement of the liquid region is higher at the top. This is since the heated liquid next to the right heated wall first reached the top right region of the enclosure and then advances toward the top left.

The impact of θ_f on the advancement of a PCM melting interface is shown in Fig. 12. It can be observed that an interface is shifted upwards when θ_f is reduced. This is due, as discussed earlier, to the fact that melting occurs when the surrounding temperature is greater than θ_f. Thus, for higher values of θ_f, the extent of zones in which melting occurs is reduced, and the melting zone shrinks, which results in moving down the melting interface.

The variations of the melting volume fraction *MVF*, the heated wall temperature $\theta_{b,ave}$, and the cooling effectiveness of utilizing PCM (η) are mapped in Fig. 13 as functions of time for various values of a high heat-flux γ. The trend of variation of these variables is similar in all the cases for all the values of γ. $\theta_{b,ave}$ rises sharply when the heat pulse is activated, then decreases progressively when the wall is cooled down until reaching the steady-state. It could be observed that throughout a duration, $\theta_{b,ave}$ increases with γ and is maximum for γ=6, as the lower wall is exposed to higher heat flux. Similarly, the MVF increases in the earlier stage of the heat pulse then decrease slowly. Due to the increased heat flux, more PCM undergoes melting for higher values of γ. On the other side, η rises drastically at the beginning of a heat pulse, so drops slowly after a pulse is deactivated while staying above 1, before decreasing sharply to a value below unity. In

fact, the efficiency is calculated by comparing the hot wall between the case with PCM to the case where the external flow effectively cools the PCM. The heat, emitted into the cavity during the active heat pulse, is initially absorbed as sensible heat, then as a latent heat when a PCM undergoes a change in its phase. When the heat pulse is deactivated, the presence of the PCM acts as a barrier among a hot wall & an exterior cooling flow. So a PCM reduces efficiency. However, the efficiency increases with γ as more heat is being absorbed. It is also clear that the effect of γ almost vanishes in a steady state.

The streamlines and the isotherms for various values of γ are depicted in Fig. 14 at different instants. It is shown that for all the instants, the size of the recirculation zone is increased when γ is increased. As more heat is emitted into the cavity, more PCM undergoes melting, and the convective flow intensifies. It can also be seen that the temperature in the cavity also increases for higher values of γ.

Fig. 15 shows the time history of $\theta_{b,ave}$, MVF, and η for various values of the characteristic lengths of the side walls S_w, S_b, and S_t. In this figure, S_w is kept constant while the two other dimensions are altered. It could be observed that such alteration has a very minor impact upon the considered variables. $\theta_{b,ave}$ is relatively lower, and the efficiency is relatively higher when S_b=S_t, i.e., when the upper and lower wall has the same thickness.

The effect of S_w, S_b, and S_t on the variations of $\theta_{b,ave}$, MVF, and η as functions of time is illustrated in Fig. 16. Here, these three dimensions are varied in a way that the total area of the cavity walls is kept constant. It can be seen that the lowest value of $\theta_{b,ave}$ is obtained when S_b and S_t are minimized, as less thermal resistance is occurring between the hot wall and the cooling fluid surrounding it. Similarly, MVF is also at its lowest in that case due to the limitation of the flow

occurrence near the sidewalls of the enclosure. Finally, the effect of these dimensions on the heat dissipator efficiency remains limited.

The variations of $\theta_{b,ave}$, MVF, and η as functions of time are mapped in Fig. 17 for several values of Rayleigh number *Ra*. $\theta_{b,ave}$ decreases with the rise of *Ra* and is minimum when $Ra=5.10^7$. Conversely, MVF is maximum for that value of *Ra*. Indeed, *Ra* signifies a relative of buoyancy forces compared to the viscous forces. When *Ra* is increased, a buoyancy-driven convective flow is strengthened, and more heat transfer occurs, cooling down the hot wall and enhancing the melting of a PCM. Consequently, the heat dissipator's efficiency also increases during a heat pulse and reaches its maximum for $Ra=5\times10^7$.

Fig. 18 depicts the time history of $\theta_{b,ave}$, MVF, and η for various values of θ_f. It is shown that MVF increases for lower θ_f while $\theta_{b,ave}$ is reduced. The efficiency is also slightly higher when θ_f is lowered. As discussed in Fig. 9, increasing θ_f reduces the zone in the cavity in which the PCM undergoes a phase change and, thus, reduces the MVF. As less PCM is contributing to a transfer of heat when an MVF is reduced, the efficiency of a heat dissipator decreases, and the lower wall remains at a higher temperature.

Fig. 19 illustrates the impact of Biot number on the variations of $\theta_{b,ave}$, MVF, and η as functions of time. It is clear that all these variables increase when *Bi* is reduced and are at their maximum for *Bi*=1.5. This can be attributed to the definition of *Bi* itself. In fact, *Bi* indicates the relative significance of the exterior cooling flow. Reducing *Bi*, thus, diminishes the heat transfer with the exterior cooling flow and, as a consequence, $\theta_{b,ave}$ rises. At the same time, such a reduction in *Bi* enhances the relative importance of the PCM phase change and its contribution to heat transfer. As the efficiency is based on a comparison of the considered cavity to the case of direct cooling with the external flow, it increases when *Bi* is lowered, i.e., when the importance of

exterior cooling is diminished. In the case of Bi=1.5, the efficiency during the pulse load is higher than 1.75. This denotes a 175% reduction in the temperature of the heated surface by using the PCM heat dissipator instead of direct cooling.

Figs. 20 and 21 summarize the effects of the various considered parameters, Bi, γ, Ra, and θ_f on the variations of $\theta_{b,ave}$, MVF, and η. It is shown that η is reduced for greater values of Bi. In addition, the impact of Bi on MVF and $\theta_{b,ave}$ is the same for all the values of Ra. They both increase when Bi is reduced, and they are maximum for Bi=1.5. Moreover, Fig. 20 shows that varying γ does not change the effect of Bi on $\theta_{b,ave}$, MVF, as both these parameters increase when Bi is lowered. In Fig. 21, it can be seen that θ_f=0.5 provides the highest MVF.

5. Conclusion

The thermal operational efficiency of a vertically mounted PCM-heat dissipator was studied in the presence of a step pulse heat-flux. The governing equations for flow & transfer of heat within a heat dissipator were introduced based on the enthalpy-porosity approach. The FEM connected with a mesh adaptation technique was employed to track a phase change interface accurately. The validations were carried out by evaluation of the outcomes by mathematical & experimental data obtainable in the literature. The simulation results were plotted for the efficiency, melting volume fraction, & average wall temperature of a hot wall. The temperature contours, streamlines, and melting regions were also plotted better to understand the complex physics of phase change heat transfer. The key findings of the current research are as follows:

- Increasing a pulse amplitude γ raises the temperature of a hot wall & a melt volume fraction MVF of a PCM, as more heat is being transferred to the cavity. The increase in the MVF enhances the impact of a PCM on a total transfer of heat, which translates into an improvement of a heat dissipator efficiency η.

- The phase change temperature of a PCM θ_f plays an important part in the thermal behavior of the PCM. Utilizing higher values of θ_f reduces the zones of the enclosure in which the PCM undergoes a phase change and decreases the MVF. Consequently, the efficiency of the heat dissipator is reduced, and the temperature of the hot wall increases.
- Raising Rayleigh number *Ra* boosts a comparative significance of the buoyancy forces compared to the viscous forces and enhances the convective impacts. As a consequence, *MVF* increases, and the hot wall temperature is reduced. Nonetheless, the effect of *Ra* on efficiency is relatively limited.
- Reducing Biot number *Bi* increases *MVF* and enhances a competence of a heat dissipator, as this number is a sign of a magnitude of convection by an exterior cooling flow. In the case of *Bi*=1.5, using the PCM heat dissipator could lead to a 175% reduction in the temperature of the heated surface.
- Minimizing the thickness of the top & bottom walls and maximizing that of the side walls decreases the hot wall's temperature due to a decreased thermal resistance. It also reduces the MVF as the flow of the melted PCM is limited near the side walls. In all the cases, the effect of the thickness of the wall on the efficiency remains limited.

Author Contributions:

M. Ghalambaz: Conceptualization, Methodology, Software, Validation, Formal analysis, Data Curation, Supervision. **S.A.M. Mehryan:** Visualization, Original draft preparation, Investigation, Formal analysis, Data Curation. **S. R. Ramazani:** Methodology, Software; Formal analysis, Data Curation. **A. Hajjar:** Investigation. Formal analysis, Writing - Review & Editing. **M. Al Kadri:** Conceptualization, Investigation, Writing - Review & Editing. **M. Saidul Islam:** Investigation,

Writing - Review & Editing. **O. Younis:** Conceptualization, Writing - Review & Editing, Investigation. **M. Ghodrat:** Writing - Review & Editing.

Data Availability Statement:

All data have been included in the paper.

Acknowledgments

This study is supported via funding from Prince Sattam Bin Abdulaziz University project number (PSAU/2023/R/1444)

List of tables:

Table 1 PCM and Aluminum foam [31, 59] thermophysical properties

Material	ρ **(kg.m^{-3})**	C_p **(J.kg^{-1}.K^{-1})**	**k (w.m^{-1}.K^{-1})**	T_l **(°C)**	T_s **(°C)**	μ **(kg.m^{-1}.s^{-1})**	β **(K^{-1})**	h_{fs} **(kJ.kg^{-1})**
PCM	900	2300	0.3	30	28	0.00324000	0.00	148.8
						0	05	
Aluminum	2719	871	202.4	-	-	-	-	

Table 2 The specifics of the tested grids when $Ra = 3.7315\times10^{7}$, $Da = 1.2\times10^{-5}$, $Bi = 2.2989$, $\varepsilon = 0.9486$, $\theta_f = 0.62637$, $\gamma = 3$

Elements number	**Case I**	**Case II**	**Case III**	**Case IV**	**Case V**
Domain	3696	4412	6670	8064	20840
Boundary	392	436	600	652	780

Table 3 Evaluated values of Nusselt number in the present study and literature works [47-52, 60]. A non-uniform grid of size 230×230 with an element ratio 20 was used for the computations.

Authors	***Ra***			
	10	**100**	**1000**	**10000**
Bejan [47]		4.200	15.800	50.8
Gross et al. [49]		3.141	13.448	42.583
Beckermann et al. [48]		3.113		48.9
Moya et al. [50]	1.065	2.801		
Sheremet and Pop [60]	1.071	3.104	13.839	49.253
Baytas and Pop [52]	1.079	3.160	14.060	48.330
Manole and Lage [51]		3.118	13.637	48.117
Present results	1.080	3.111	13.642	48.561

610 **List of figures**

611

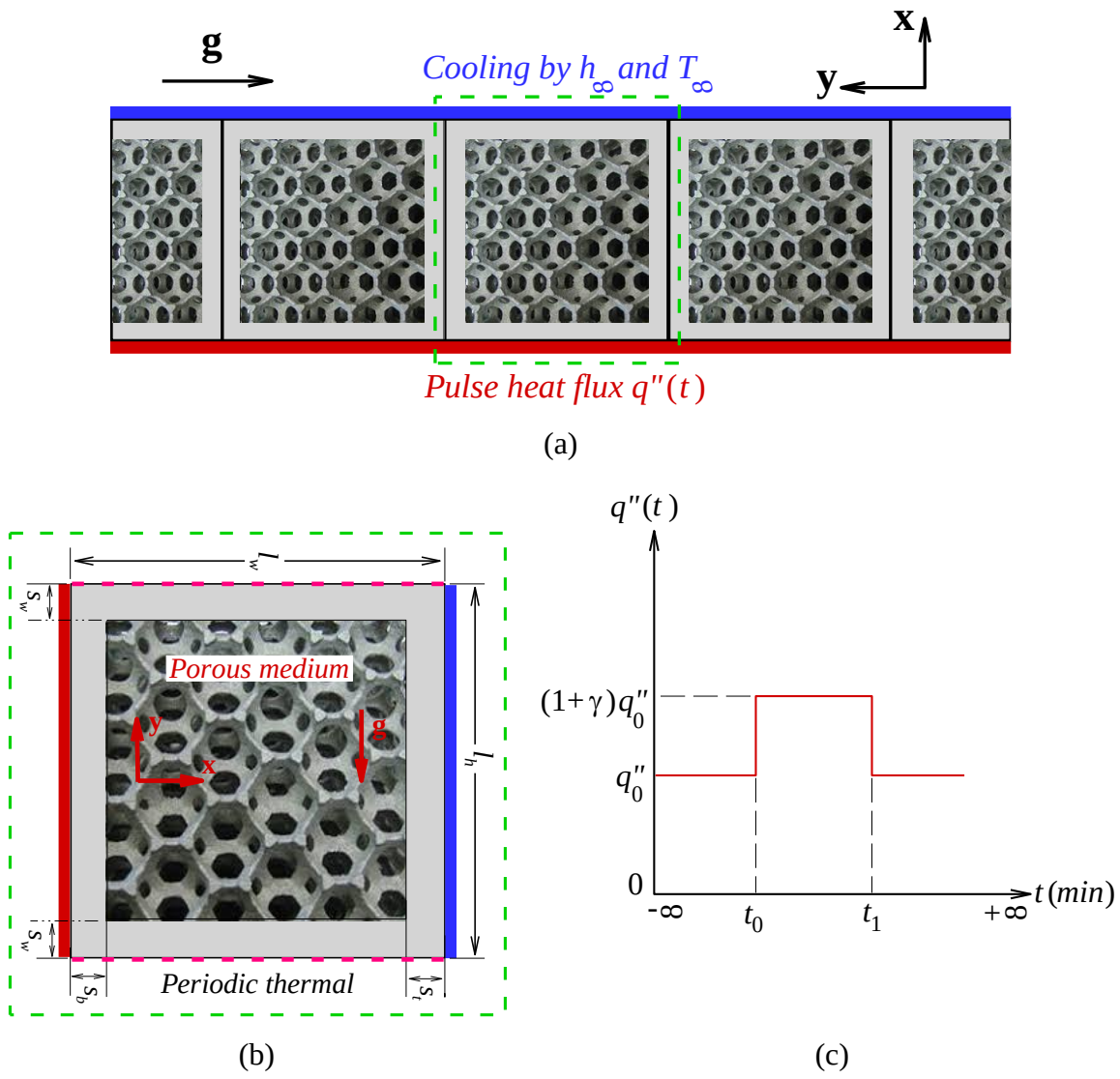

612 **Fig. 1.** The heat dissipator is plotted horizontally while the the gravity is acting against y
613 direction. Thus, the heat dissipator is actually analyzed vertically. The model of the composite
614 heat dissipator; (a): A view of the vertical heat dissipator ad cell arrangements; (b): A
615 comprehensive view of a single cell and its geometry specifications; (c): a profile of heat-flux

616

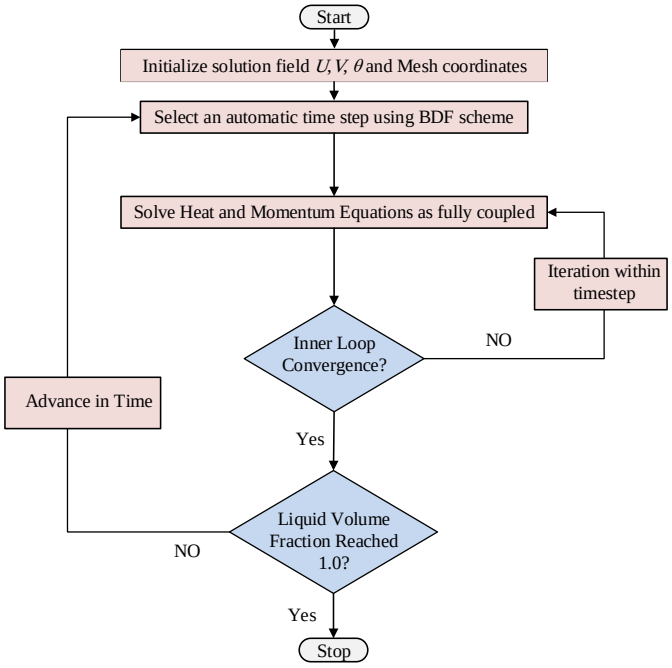

Fig. 2. Flow chart of the used numerical method

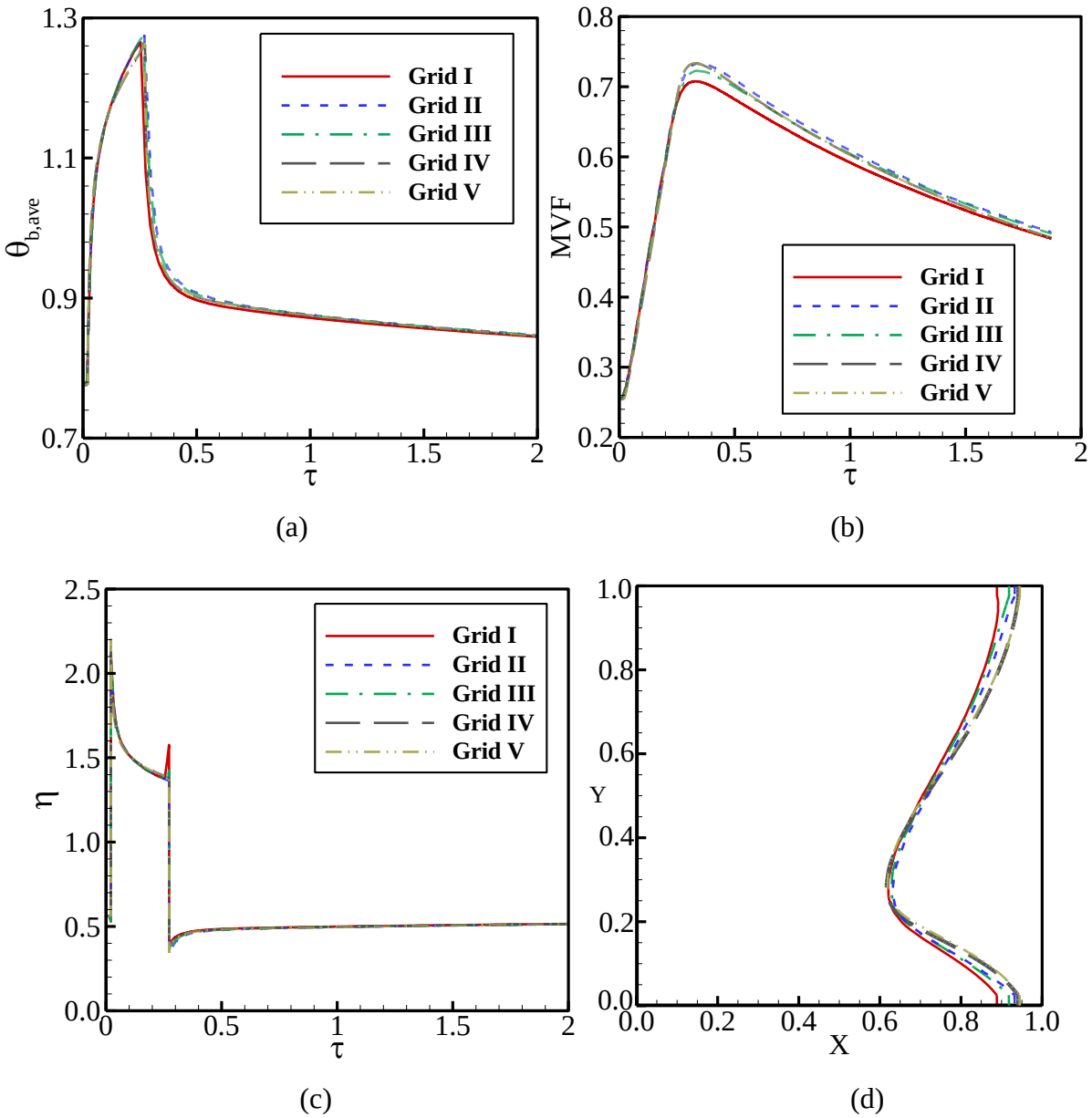

Fig. 3. The impact of investigated grids on (a): the bottom surface temperature, (b): the molten fraction (*MVF*), (c): the phase transition heat transfer efficiency, and (d): the melting interface at $\tau = 0.3148$

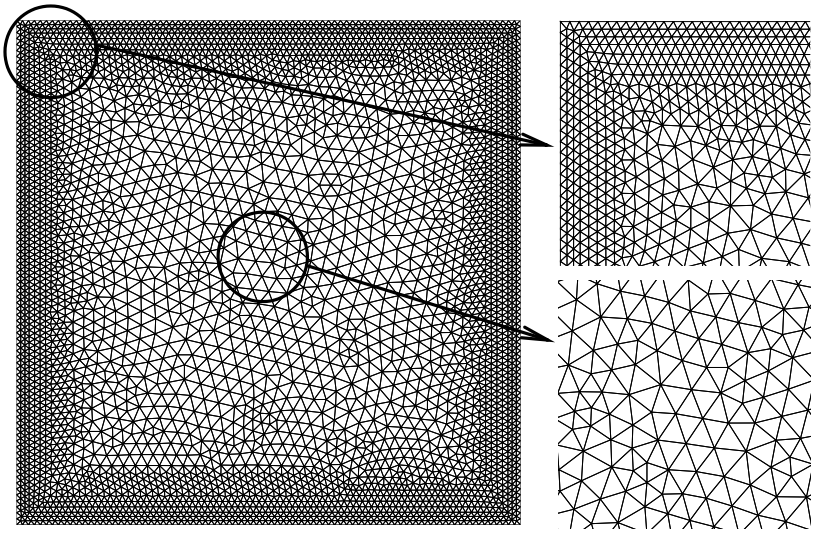

628

629 **Fig. 4.** An illustration of the computations grid (Grid IV).

630

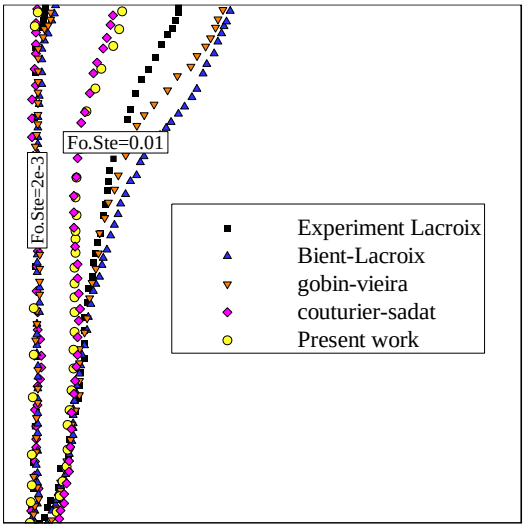

631

632 **Fig. 5.** A comparison among the outcomes of a the current research & literature review of [54]

633

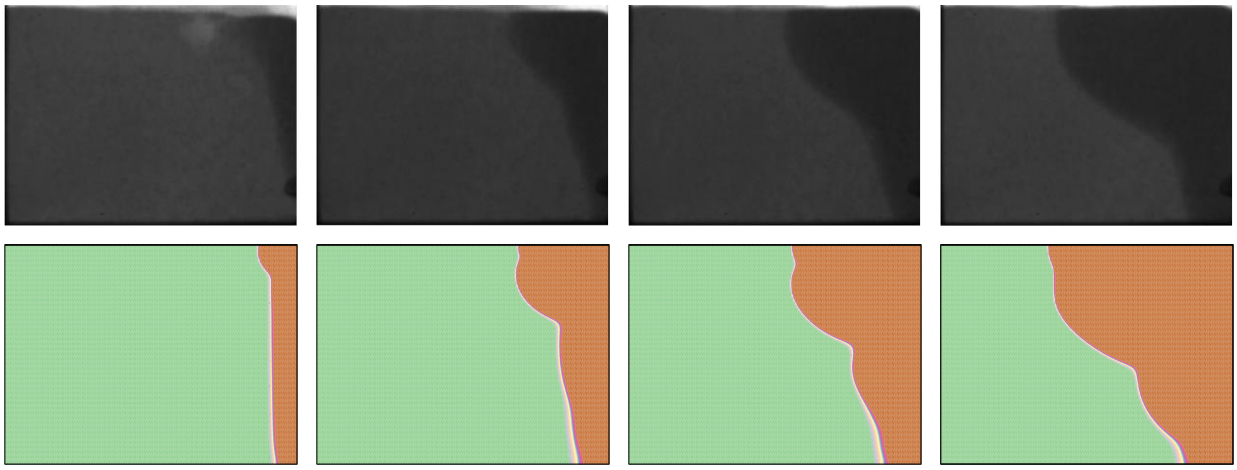

(a) (b) (c) (d)

634 **Fig. 6.** The experimental reuslts of Kumar et al. [53] & the mathematical outcomes of the current

635 work for (a): τ = 0.37, (b): τ = 0.73, (c): τ = 1.10 and (d): τ = 1.47

636

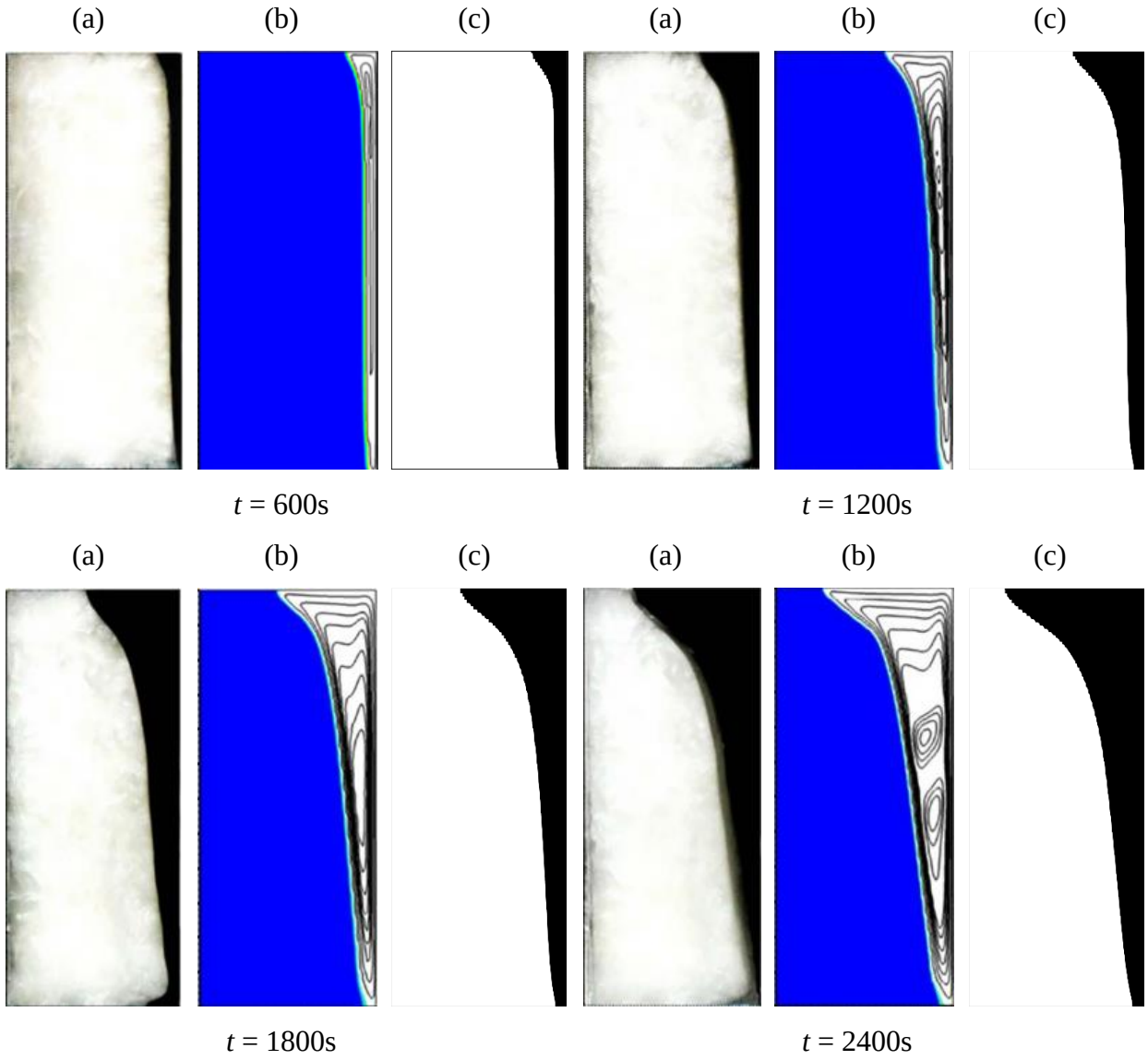

637 **Fig. 7.** Melting fields of (a) experimental study presented in [55], (b) numerical study presented in

638 [55], and (c) present work; $Ra = 8.3\times10^{8}$, $Ste = 0.52$, $Pr = 100.7$

639

640

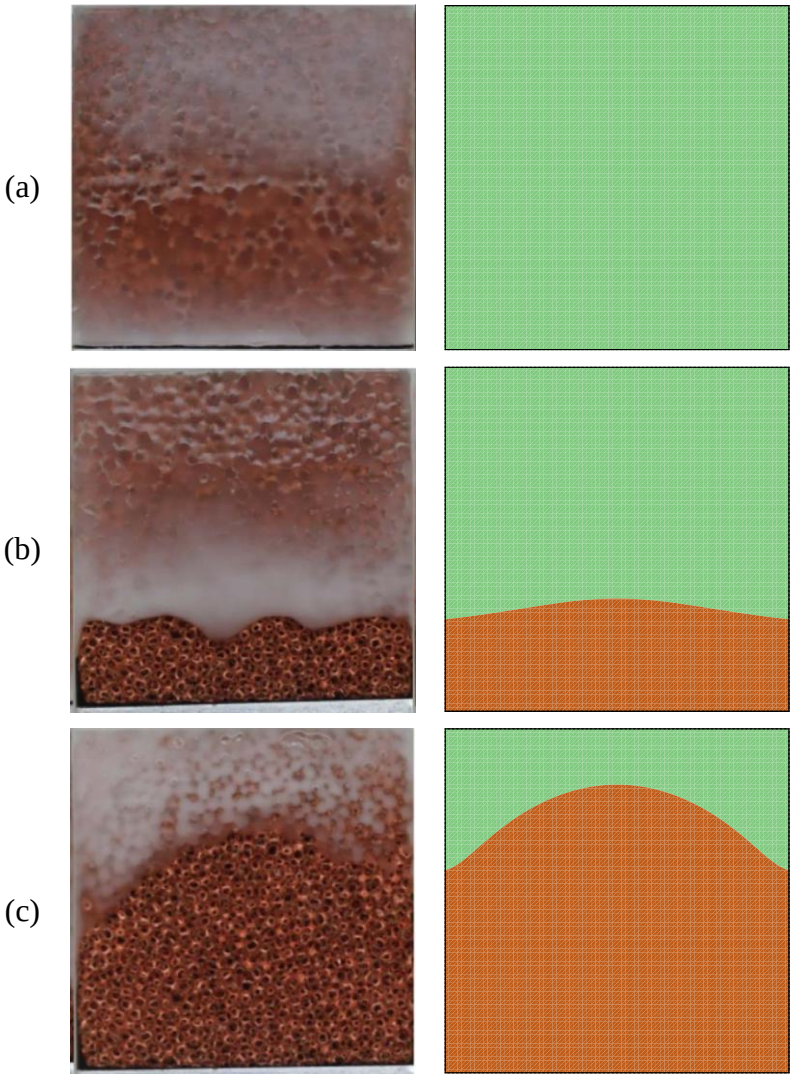

641

642 **Fig. 8.** The outcomes exhibited in [31] and the numerical outcomes of the current work for (a): t

643 = 5400 s (b): t = 10800 s and (c): t = 16200 s

644

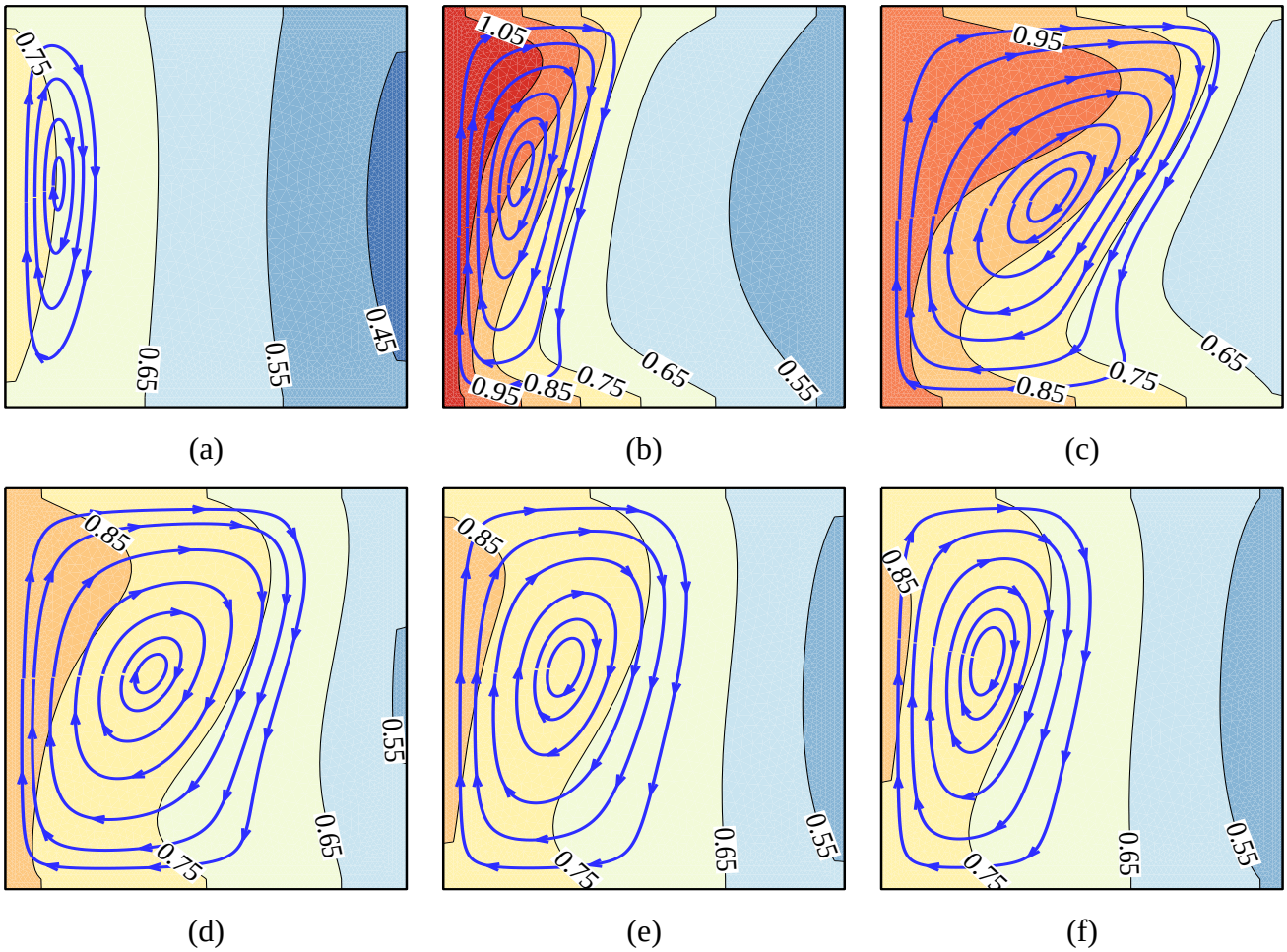

(a) (b) (c)

(d) (e) (f)

Fig. 9. The isotherms and streamlines for selected dimensionless time steps (τ) when Bi = 2.2989, θ_f = 0.626 and γ = 3; (a): τ = 0 (t = 0s); (b): τ = 0.1049 (t = 500s); (c): τ = 0.3148 (t = 1500s); (d): τ = 0.6296 (t = 3000s); (e): τ = 1.259 (t = 6000s); (f): τ = 1.8887 (t = 9000s).

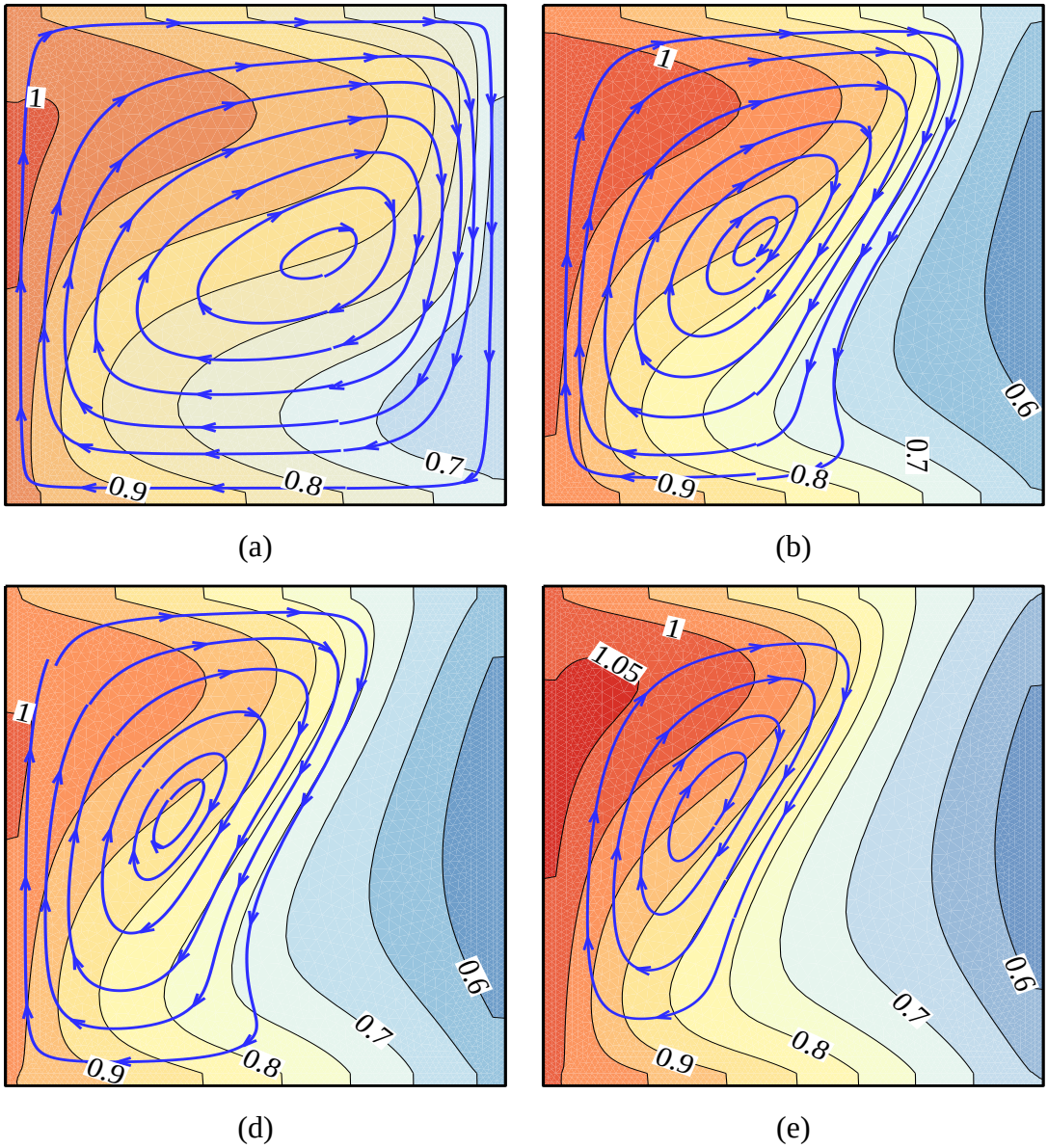

649 **Fig. 10.** The temperature map and streamlines for selected dimensionless phase change
650 temperatures (θ_f) when Bi = 2.2989, τ = 0.3148 (t = 1500s) and γ = 3; (a)*:* θ_f = 0.539 (MVF =
651 0.902 and $\theta_{b,ave}$ = 0.991); (b)*:* θ_f = 0.626 (MVF = 0.716 and $\theta_{b,ave}$ = 1.021); (c): θ_f = 0.661 (MVF =
652 0.611 and $\theta_{b,ave}$ = 0.984); and (d): θ_f = 0.696 (MVF = 0. 561 and $\theta_{b,ave}$ = 0.418);

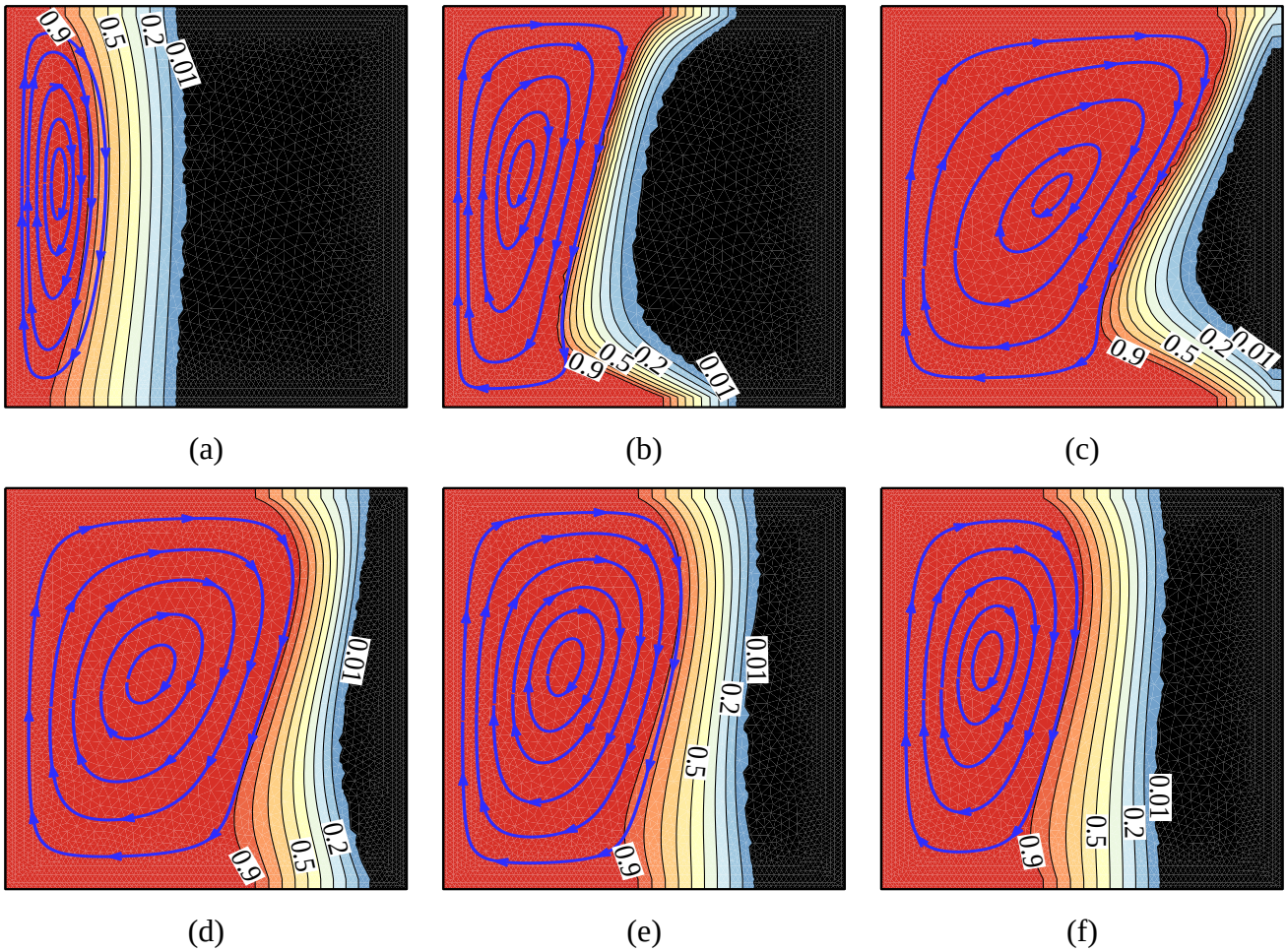

Fig. 11. The contours of melting fraction and streamlines for selected dimensionless time steps (τ) when Bi = 2.2989, θ_f = 0.626 and γ = 3; (a): τ = 0 (t = 0s); (b): τ = 0.1049 (t = 500s); (c): τ = 0.3148 (t = 1500s); (d): τ = 0.6296 (t = 3000s); (e): τ = 1.259 (t = 6000s); (f): τ = 1.8887 (t = 9000s).

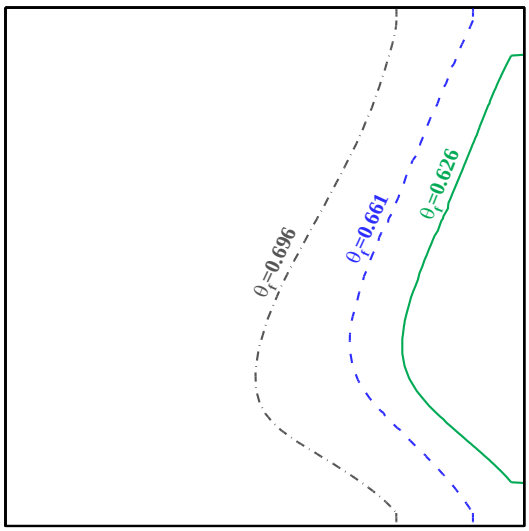

Fig. 12. The melting interface for selected dimensionless phase change temperatures (θ_f) when τ = 0.3148, Bi = 2.2989, Ra = 3.7315×10^{7}, Da = 1.2×10^{-5}, and γ = 3

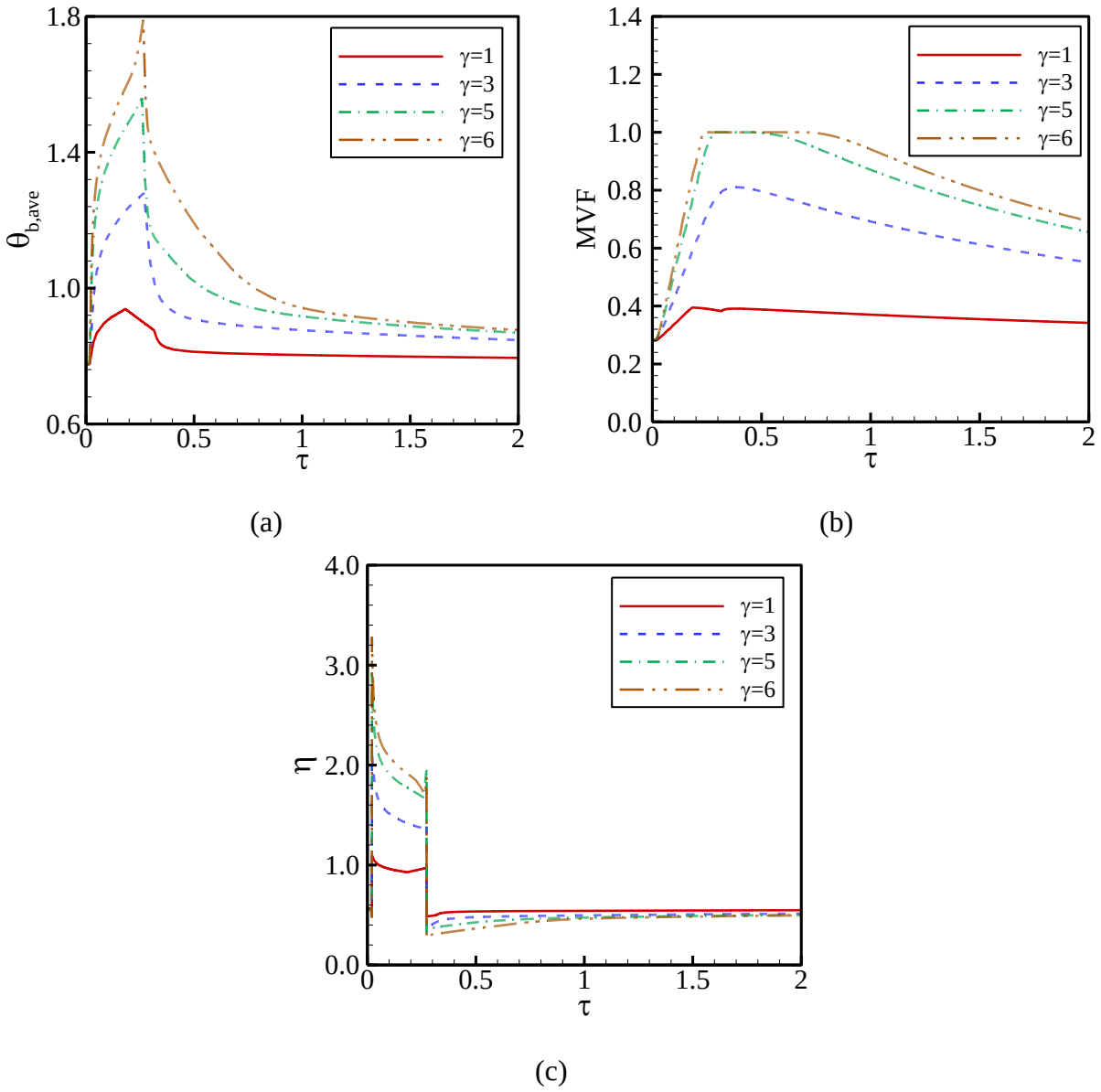

Fig. 13. The change of distinctive factors throughout the heat pulse for selected magnetudes of heat flux (γ) when θ_f = 0.626, Bi = 2.2989, Ra = 3.7315×10^7, Da = 1.2×10^{-5}; (a): the bottom surface temperature; (b): the molten fraction (*MVF*), and (c): the phase change heat transfer efficiency $\boldsymbol{\eta}$.

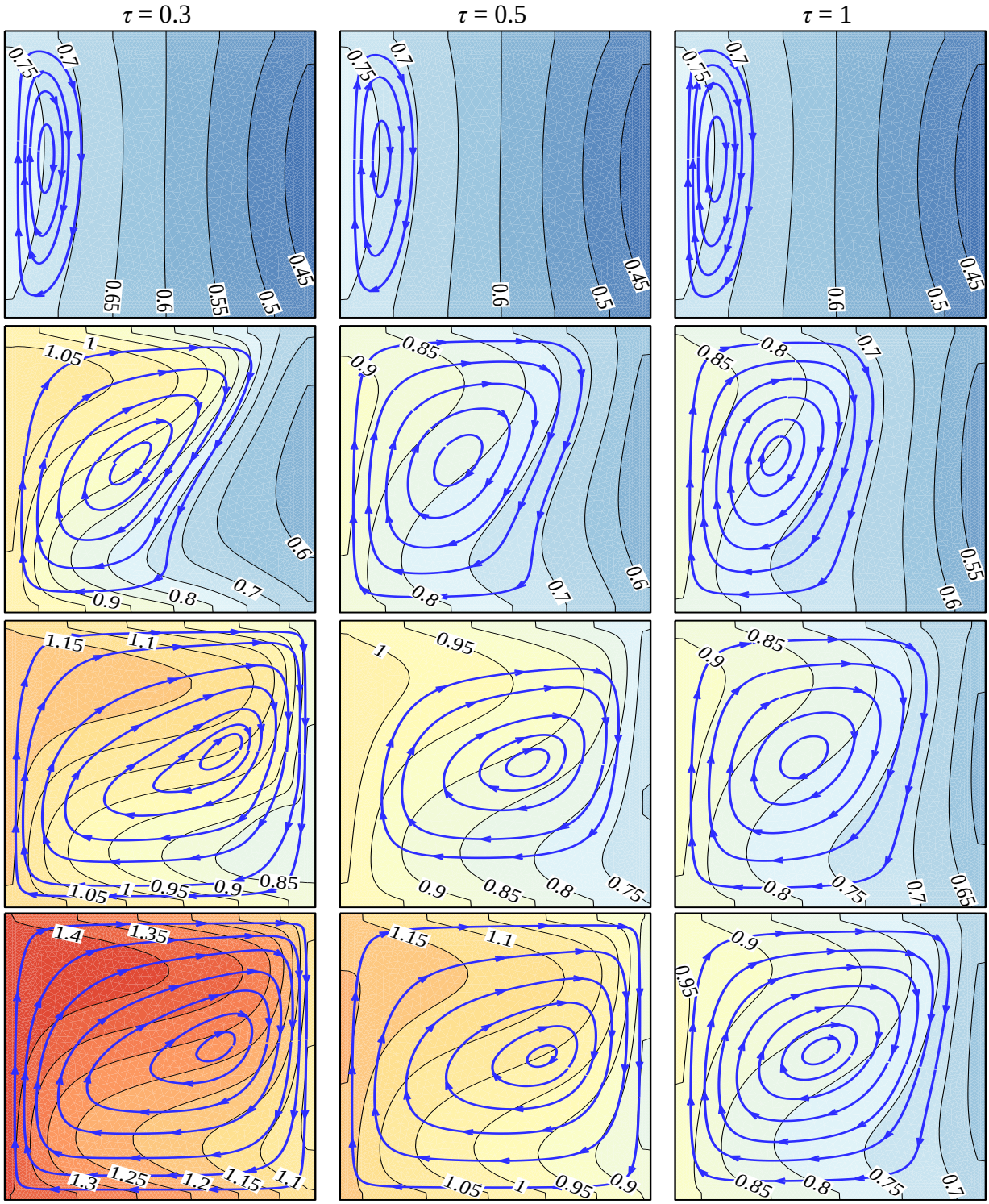

Fig. 14. The temperature distribution and streamlines and three values of non-dimensional time (τ); (a)*:* γ = 0; (b)*:* γ = 3; (c): γ = 5; (d): γ =6; when Bi = 2.2989, θ_f = 0.626, Ra = 3.7315×10^7 and Da = 1.2×10^{-5}.

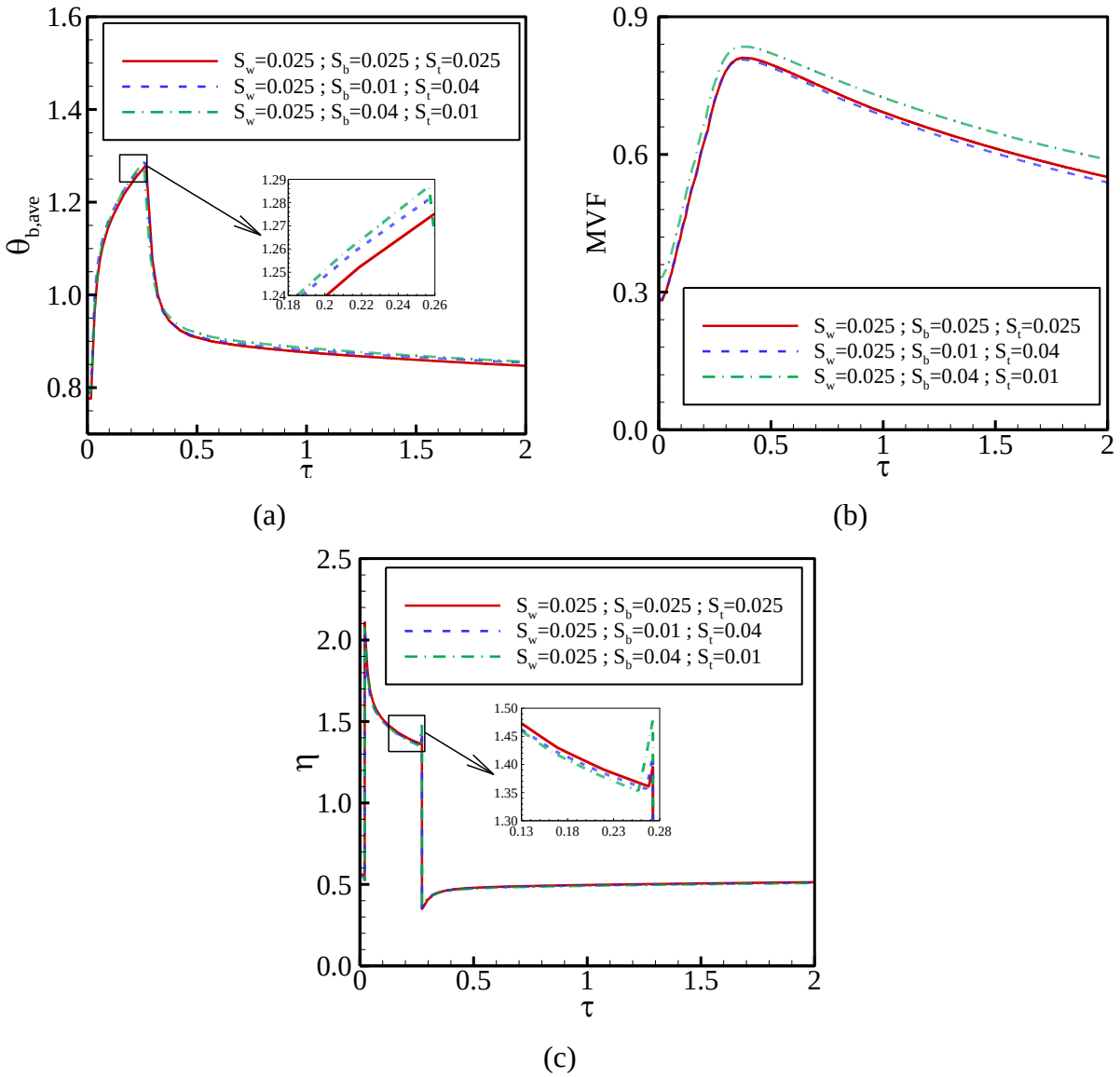

Fig. 15. The difference of distinctive factors throughout a heat pulse & afterwards a heat pulse for selected characteristics lengths (S_w, S_b, S_t) when θ_f = 0.626, Bi = 2.2989, Ra = 3.7315×10^7, Da = 1.2×10^{-5} and γ = 3; (a): the bottom surface temperature; (b): the molten fraction (MVF), and (c): the phase change heat transfer efficiency $\boldsymbol{\eta}$.

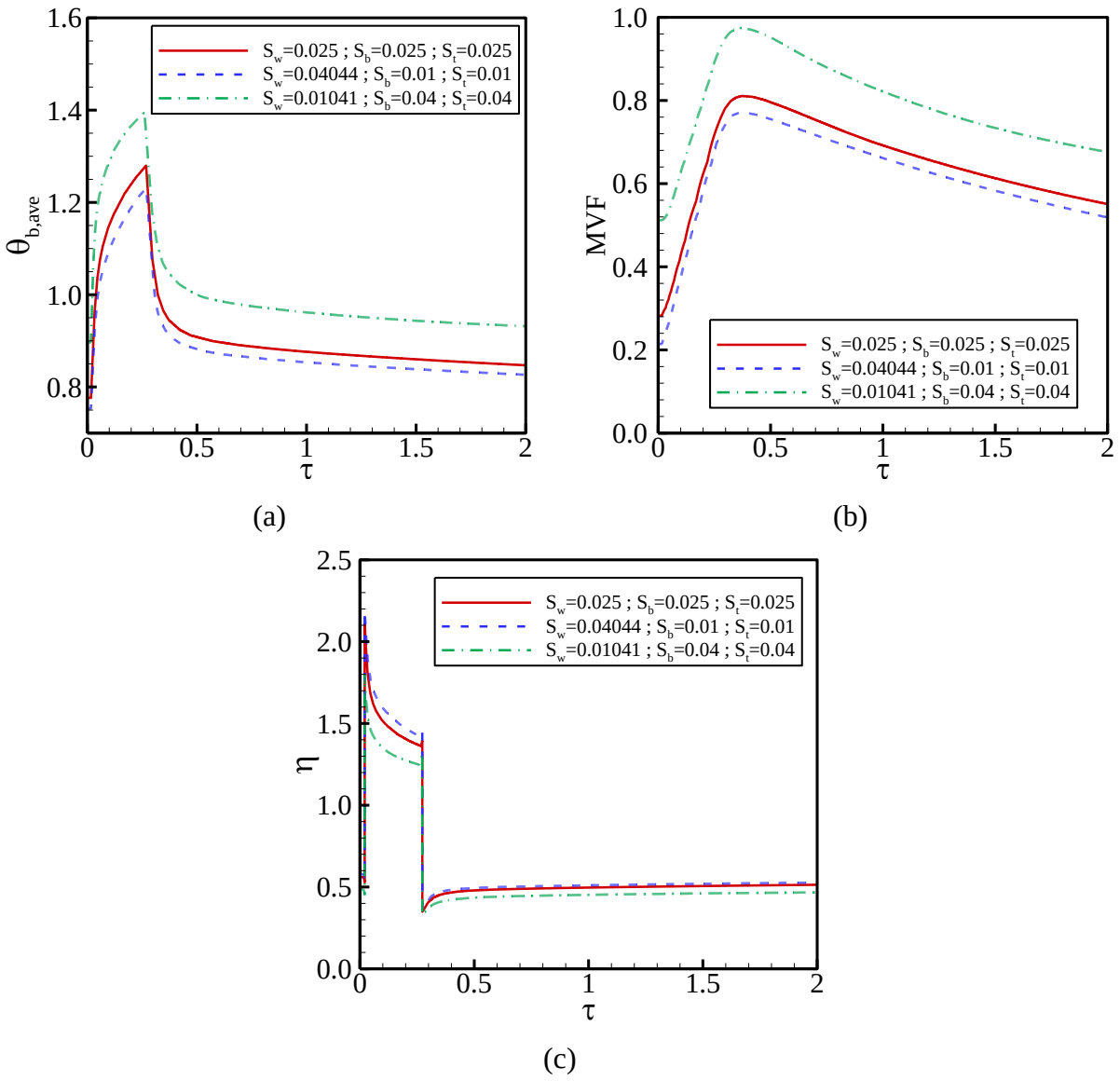

Fig. 16. Effect of a difference of S_w throughout a heat pulse & afterwards the heat pulse for selected characteristic lengths (S_w, S_b, S_t) when θ_f = 0.626, Bi = 2.2989, Ra = 3.7315×10^7, Da = 1.2×10^{-5} and γ = 3; (a): the bottom surface temperature; (b): the molten fraction (MVF), and (c): the phase change heat transfer efficiency $\boldsymbol{\eta}$.

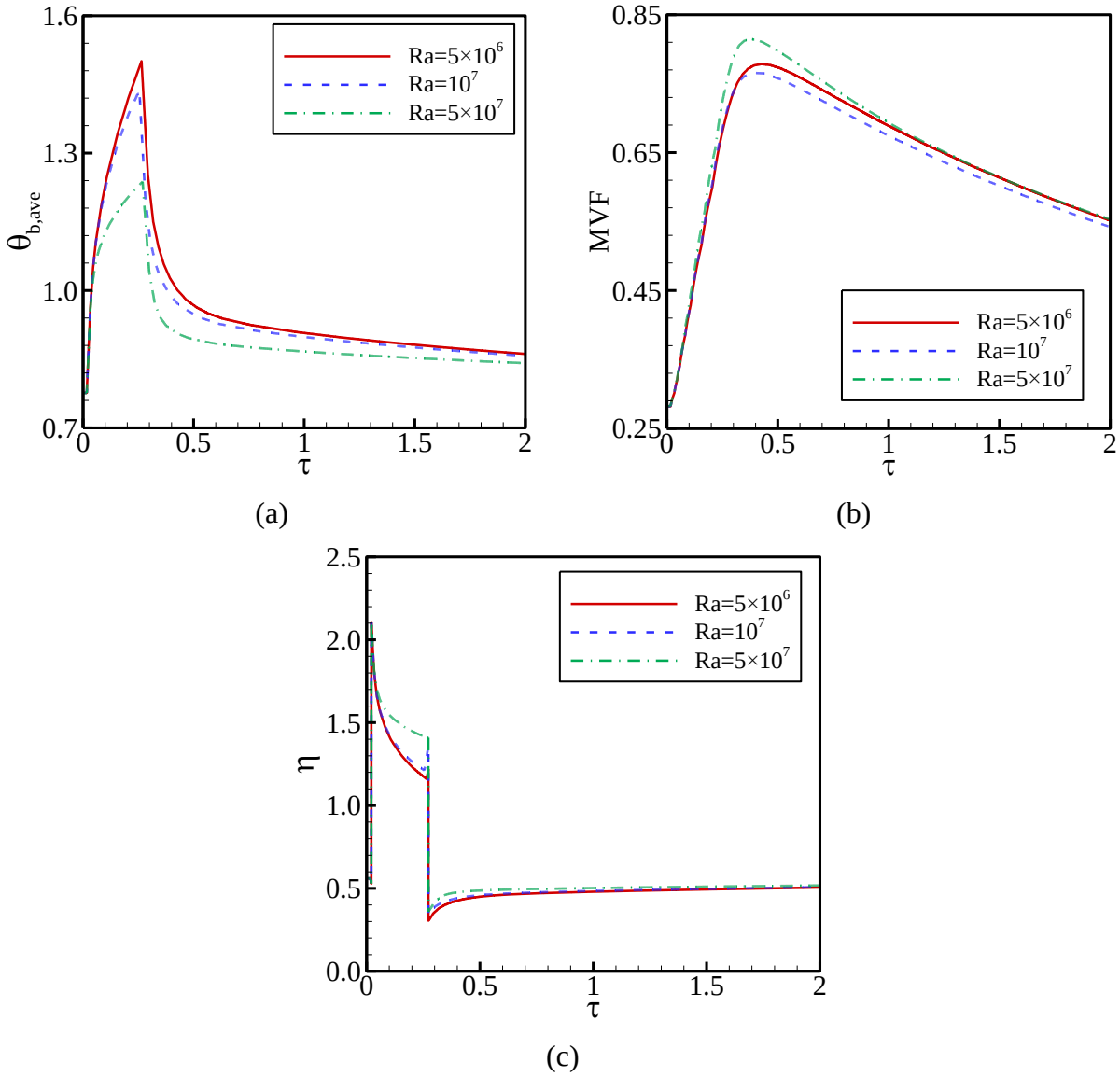

Fig. 17. The difference of distinctive factors throughout a heat pulse & afterwards the heat pulse for selected Rayleigh numbers (*Ra*) when $\theta_f = 0.626$, $Bi = 2.2989$, $Da = 1.2\times10^{-5}$ and $\gamma = 3$; (a): the bottom surface temperature; (b): the molten fraction (*MVF*), and (c): the phase change heat transfer efficiency $\boldsymbol{\eta}$.

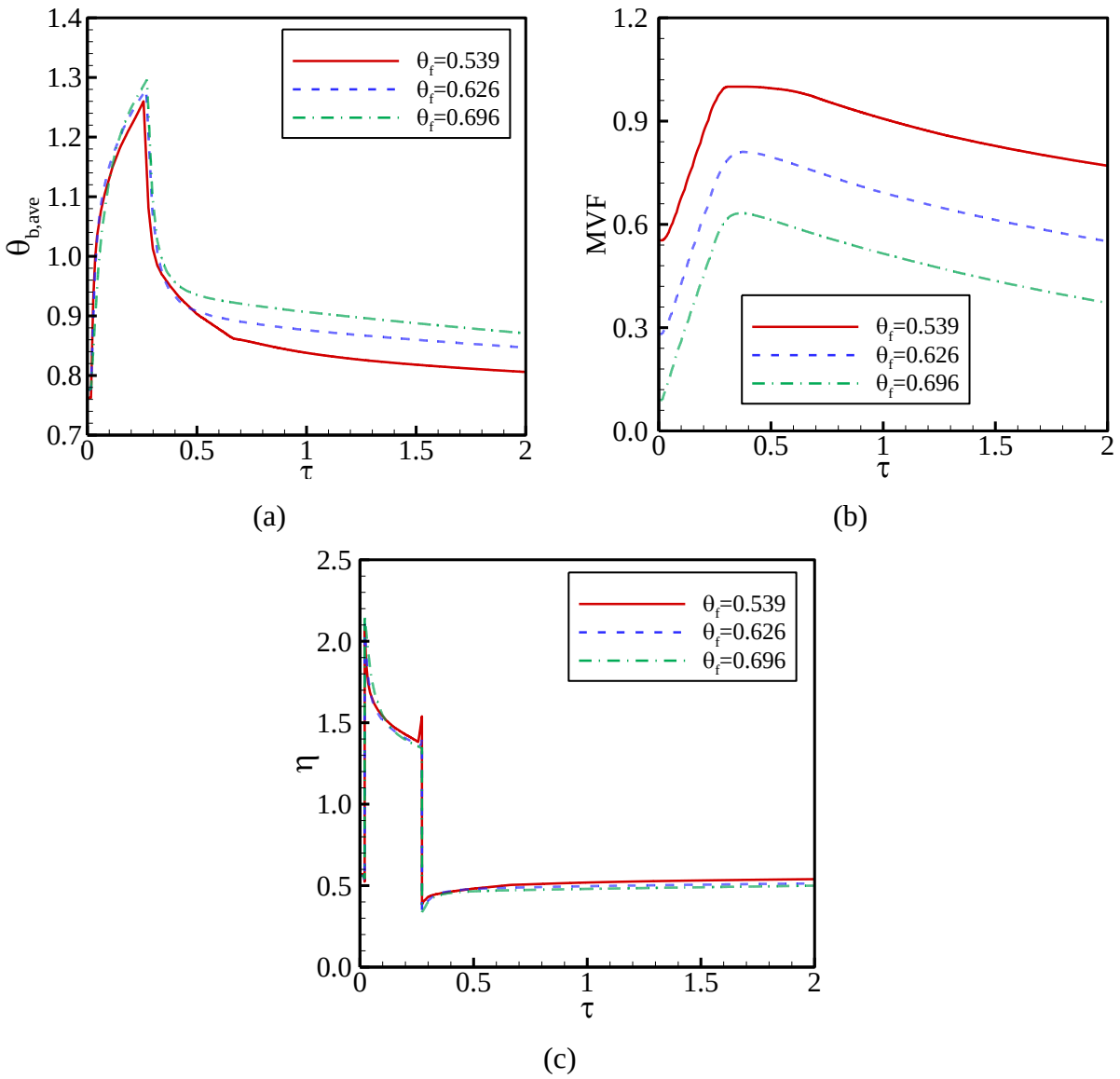

Fig. 18. The difference of distinctive factors throughout a heat pulse & afterwards the heat pulse for selected phase change temperatures (θ_f) when Bi = 2.2989, Ra = 3.7315×10^7, Da = 1.2×10^{-5} and γ=3; (a): the bottom surface temperature; (b): the molten fraction (MVF), and (c): the phase change heat transfer efficiency η.

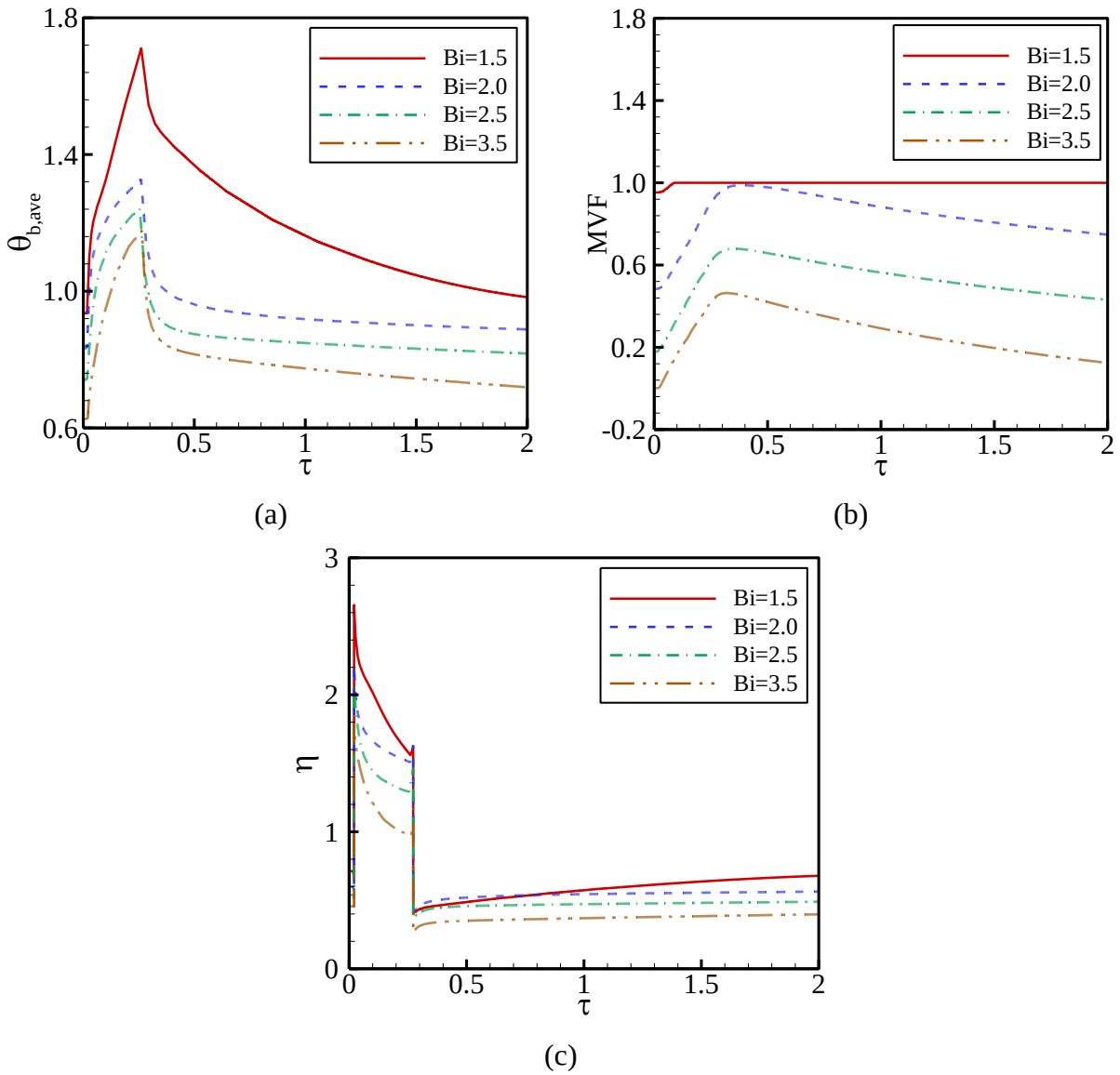

Fig. 19. The difference of distinctive factors throughout a heat pulse & afterwards the heat pulse for selected Biot numbers (*Bi*) when $\theta_f = 0.626$, $Ra = 3.7315\times10^{7}$, $Da = 1.2\times10^{-5}$ and $\gamma = 3$; (a): the bottom surface temperature; (b): the molten fraction (*MVF*); and (c): the phase change heat transfer efficiency $\boldsymbol{\eta}$.

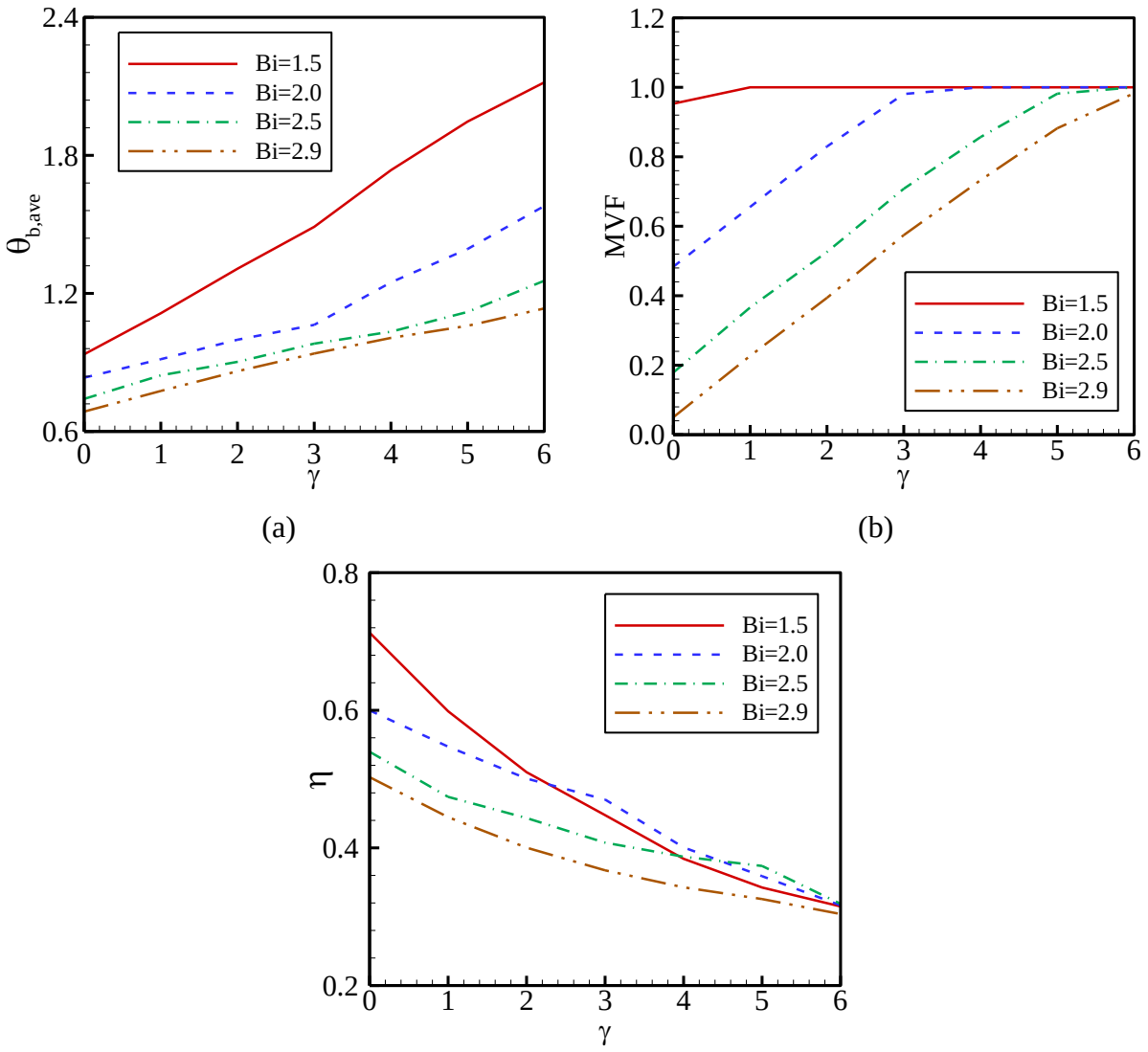

712 **Fig. 20.** The difference of distinctive factors as a function of γ for selected Biot number (*Bi*)

713 when $\theta_f = 0.626$, $Da = 1.2\times10^{-5}$, $Ra = 3.7315\times10^{7}$ and $\tau = 0.3148$; (a): the bottom surface

714 temperature; (b): the molten fraction (*MVF*), and (c): the phase change heat transfer efficiency

715 η.

716

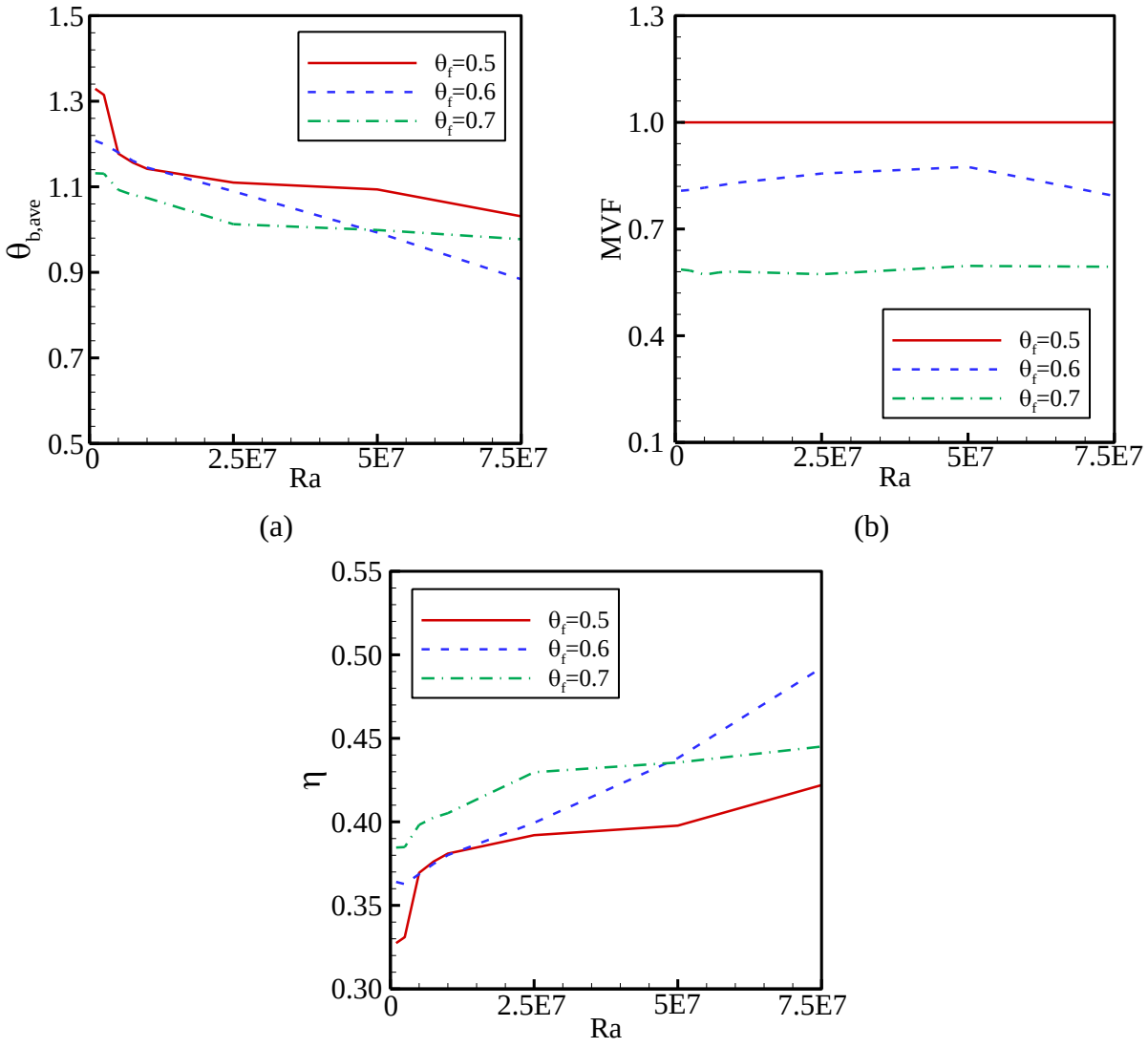

Fig. 21. The variation of characteristic parameters as a function of *Ra* for selected phase change temperaturs (θ_f) when Bi = 2.2989, Da = 1.2×10^{-5}, γ = 3, and τ = 0.3148; (a): the bottom surface temperature; (b): the molten fraction (*MVF*), and (c): the phase change heat transfer efficiency η.

References

[1] A.M. Rashad, T. Armaghani, A.J. Chamkha, M.A. Mansour, Entropy generation and MHD natural convection of a nanofluid in an inclined square porous cavity: Effects of a heat sink and source size and location, Chinese Journal of Physics, 56(1) (2018) 193-211.

[2] M. Sheikholeslami, S.A.M. Mehryan, A. Shafee, M.A. Sheremet, Variable magnetic forces impact on magnetizable hybrid nanofluid heat transfer through a circular cavity, Journal of Molecular Liquids, 277 (2019) 388-396.

[3] A.I. Alsabery, M.A. Ismael, A.J. Chamkha, I. Hashim, Effect of nonhomogeneous nanofluid model on transient natural convection in a non-Darcy porous cavity containing an inner solid body, International Communications in Heat and Mass Transfer, 110 (2020).

[4] P. Sreedevi, P.S. Reddy, K. Suryanarayana Rao, Effect of magnetic field and radiation on heat transfer analysis of nanofluid inside a square cavity filled with silver nanoparticles: Tiwari–Das model, Waves in Random and Complex Media, (2021) 1-19.

[5] A. Alsabery, M. Sheremet, M. Sheikholeslami, A. Chamkha, I. Hashim, Magnetohydrodynamics energy transport inside a double lid-driven wavy-walled chamber: Impacts of inner solid cylinder and two-phase nanoliquid approach, International Journal of Mechanical Sciences, 184 (2020) 105846.

[6] S. Rajput, A.K. Verma, K. Bhattacharyya, A.J. Chamkha, Unsteady nonlinear mixed convective flow of nanofluid over a wedge: Buongiorno model, Waves in Random and Complex Media, (2021) 1-15.

[7] A.K. Gautam, A.K. Verma, K. Bhattacharyya, S. Mukhopadhyay, A.J. Chamkha, Impacts of activation energy and binary chemical reaction on MHD flow of Williamson nanofluid in Darcy–Forchheimer porous medium: a case of expanding sheet of variable thickness, Waves in Random and Complex Media, (2021) 1-22.

[8] C.J. Ho, J.B. Huang, P.S. Tsai, Y.M. Yang, Water-based suspensions of Al2O3 nanoparticles and MEPCM particles on convection effectiveness in a circular tube, International Journal of Thermal Sciences, 50(5) (2011) 736-748.

[9] N. Alsedais, A.M. Aly, Double-diffusive convection from an oscillating baffle embedded in an astroid-shaped cavity suspended by nano encapsulated phage change materials: ISPH simulations, Waves in Random and Complex Media, (2021) 1-20.

[10] A.M. Aly, Z. Raizah, S. El-Sapa, H.F. Oztop, N. Abu-Hamdeh, Thermal diffusion upon magnetic field convection of nano-enhanced phase change materials in a permeable wavy cavity with crescent-shaped partitions, Case Studies in Thermal Engineering, 31 (2022) 101855.

[11] N. Mallya, S. Haussener, Buoyancy-driven melting and solidification heat transfer analysis in encapsulated phase change materials, International Journal of Heat and Mass Transfer, 164 (2021) 120525.

[12] M. Gürtürk, B. Kok, A new approach in the design of heat transfer fin for melting and solidification of PCM, International Journal of Heat and Mass Transfer, 153 (2020) 119671.

[13] H. Ettouney, H. El-Dessouky, E. Al-Kandari, Heat transfer characteristics during melting and solidification of phase change energy storage process, Industrial & engineering chemistry research, 43(17) (2004) 5350-5357.

[14] M. Paknezhad, A.M. Rashidi, T. Yousefi, Z. Saghir, Effect of aluminum-foam heat sink on inclined hot surface temperature in the case of free convection heat transfer, Case Studies in Thermal Engineering, 10 (2017) 199-206.

[15] S. Sivasankaran, A.I. Alsabery, I. Hashim, Internal heat generation effect on transient natural convection in a nanofluid-saturated local thermal non-equilibrium porous inclined cavity, Physica A: Statistical Mechanics and its Applications, 509 (2018) 275-293.

[16] A.I. Alsabery, R. Roslan, J. Al-Smail, I. Hashim, Effects of internal heat generation and partial heating on transient natural convection in an inclined porous cavity using LTNE model, Journal of Porous Media, 23(2) (2020).

[17] S. Sivasankaran, A. Alsabery, I. Hashim, Internal heat generation effect on transient natural convection in a nanofluid-saturated local thermal non-equilibrium porous inclined cavity, Physica A: Statistical Mechanics and its Applications, 509 (2018) 275-293.

[18] A.I. Alsabery, H. Saleh, I. Hashim, Effects of viscous dissipation and radiation on MHD natural convection in oblique porous cavity with constant heat flux, Advances in Applied Mathematics and Mechanics, 9(2) (2017) 463-484.

[19] D.T. Yaseen, M.A. Ismael, Analysis of power law fluid-structure interaction in an open trapezoidal cavity, International Journal of Mechanical Sciences, 174 (2020) 105481.

[20] M.A. Ismael, H.F. Jasim, Role of the fluid-structure interaction in mixed convection in a vented cavity, International Journal of Mechanical Sciences, 135 (2018) 190-202.

[21] P. Talebizadehsardari, H.I. Mohammed, J.M. Mahdi, M. Gillott, G.S. Walker, D. Grant, D. Giddings, Effect of airflow channel arrangement on the discharge of a composite metal foam-phase change material heat exchanger, International Journal of Energy Research, (2020).

[22] P.T. Sardari, R. Babaei-Mahani, D. Giddings, S. Yasseri, M. Moghimi, H. Bahai, Energy recovery from domestic radiators using a compact composite metal Foam/PCM latent heat storage, Journal of Cleaner Production, 257 (2020) 120504.

[23] J. Baumeister, J. Weise, S. Myslicki, E. Kieseritzky, G. Lindenberg, PCM-Based Energy Storage System with High Power Output Using Open Porous Aluminum Foams, Energies, 13(23) (2020) 6198.

[24] P. Zhang, Z.N. Meng, H. Zhu, Y.L. Wang, S.P. Peng, Melting heat transfer characteristics of a composite phase change material fabricated by paraffin and metal foam, Applied Energy, 185 (2017) 1971-1983.

795 [25] A. Ghahremannezhad, H. Xu, M.R. Salimpour, P. Wang, K. Vafai, Thermal performance
796 analysis of phase change materials (PCMs) embedded in gradient porous metal foams,
797 Applied Thermal Engineering, 179 (2020) 115731.

798 [26] S. Mahjoob, K. Vafai, A synthesis of fluid and thermal transport models for metal foam heat
799 exchangers, International Journal of Heat and Mass Transfer, 51(15-16) (2008) 3701-3711.

800 [27] S. Mancin, A. Diani, L. Doretti, K. Hooman, L. Rossetto, Experimental analysis of phase
801 change phenomenon of paraffin waxes embedded in copper foams, International Journal of
802 Thermal Sciences, 90 (2015) 79-89.

803 [28] P.T. Sardari, H.I. Mohammed, D. Giddings, M. Gillott, D. Grant, Numerical study of a
804 multiple-segment metal foam-PCM latent heat storage unit: Effect of porosity, pore density
805 and location of heat source, Energy, 189 (2019) 116108.

806 [29] P.T. Sardari, D. Giddings, D. Grant, M. Gillott, G.S. Walker, Discharge of a composite metal
807 foam/phase change material to air heat exchanger for a domestic thermal storage unit,
808 Renewable Energy, 148 (2020) 987-1001.

809 [30] P.T. Sardari, D. Grant, D. Giddings, G.S. Walker, M. Gillott, Composite metal foam/PCM
810 energy store design for dwelling space air heating, Energy Conversion and Management, 201
811 (2019) 112151.

812 [31] H. Zheng, C. Wang, Q. Liu, Z. Tian, X. Fan, Thermal performance of copper foam/paraffin
813 composite phase change material, Energy conversion and management, 157 (2018) 372-381.

814 [32] M.S.M. Al-Jethelah, S.H. Tasnim, S. Mahmud, A. Dutta, Melting of nano-phase change
815 material inside a porous enclosure, International Journal of Heat and Mass Transfer, 102
816 (2016) 773-787.

817 [33] S.A. Khateeb, S. Amiruddin, M. Farid, J.R. Selman, S. Al-Hallaj, Thermal management of
818 Li-ion battery with phase change material for electric scooters: experimental validation,
819 Journal of Power Sources, 142(1-2) (2005) 345-353.

[34] Z. Wang, Z. Zhang, L. Jia, L. Yang, Paraffin and paraffin/aluminum foam composite phase change material heat storage experimental study based on thermal management of Li-ion battery, Applied Thermal Engineering, 78 (2015) 428-436.

[35] W.Q. Li, Z.G. Qu, Y.L. He, Y.B. Tao, Experimental study of a passive thermal management system for high-powered lithium ion batteries using porous metal foam saturated with phase change materials, Journal of Power Sources, 255 (2014) 9-15.

[36] Z. Ling, X. Wen, Z. Zhang, X. Fang, X. Gao, Thermal management performance of phase change materials with different thermal conductivities for Li-ion battery packs operated at low temperatures, Energy, 144 (2018) 977-983.

[37] M. Ghalambaz, J. Zhang, Conjugate solid-liquid phase change heat transfer in heatsink filled with phase change material-metal foam, International Journal of Heat and Mass Transfer, 146 (2020) 118832.

[38] A.A. Nnanna, A. Haji-Sheikh, K.T. Harris, Experimental study of local thermal non-equilibrium phenomena during phase change in porous media, International journal of heat and mass transfer, 47(19-20) (2004) 4365-4375.

[39] K. Jiao, L. Lu, T. Wen, Q. Wang, A modified mixture theory for one-dimensional melting of pure PCM and PCM/metal foam composite: numerical analysis and experiment validation, International Journal of Heat and Mass Transfer, 186 (2022) 122461.

[40] X. Hu, X. Gong, Pore-scale numerical simulation of the thermal performance for phase change material embedded in metal foam with cubic periodic cell structure, Applied thermal engineering, 151 (2019) 231-239.

[41] J.M. Mahdi, H.I. Mohammed, E.T. Hashim, P. Talebizadehsardari, E.C. Nsofor, Solidification enhancement with multiple PCMs, cascaded metal foam and nanoparticles in the shell-and-tube energy storage system, Applied Energy, 257 (2020) 113993.

[42] D.A. Nield, A. Bejan, Convection in porous media, Springer Science & Business Media, 2006.

[43] J. Buongiorno, Convective transport in nanofluids, Journal of Heat Transfer, 128(3) (2006) 240-250.

[44] M. Sheikholeslami, M. Shamlooei, R. Moradi, Fe3O4-Ethylene glycol nanofluid forced convection inside a porous enclosure in existence of Coulomb force, Journal of Molecular Liquids, 249 (2018) 429-437.

[45] O. Mesalhy, K. Lafdi, A. Elgafy, K. Bowman, Numerical study for enhancing the thermal conductivity of phase change material (PCM) storage using high thermal conductivity porous matrix, Energy Conversion and Management, 46(6) (2005) 847-867.

[46] L. Betchen, A.G. Straatman, B.E. Thompson, A nonequilibrium finite-volume model for conjugate fluid/porous/solid domains, Numerical Heat Transfer, Part A: Applications, 49(6) (2006) 543-565.

[47] A. Bejan, On the boundary layer regime in a vertical enclosure filled with a porous medium, Letters in Heat and Mass Transfer, 6(2) (1979) 93-102.

[48] C. Beckermann, R. Viskanta, S. Ramadhyani, A numerical study of non-Darcian natural convection in a vertical enclosure filled with a porous medium, Numerical Heat Transfer, 10(6) (1986) 557-570.

[49] R. Gross, M. Bear, C. Hickox, The application of flux-corrected transport (FCT) to high Rayleigh number natural convection in a porous medium, in: Proc. 8th Int. Heat Transfer Conf., San Francisco, CA, 1986.

[50] S.L. Moya, E. Ramos, M. Sen, Numerical study of natural convection in a tilted rectangular porous material, International journal of heat and mass transfer, 30(4) (1987) 741-756.

[51] D.M. Manole, Numerical benchmark results for natural convection in a porous medium cavity, in: Heat and Mass Transfer in Porous Media, ASME Conference 1992, 1992, pp. 55-60.

[52] A.C. Baytas, I. Pop, Free convection in oblique enclosures filled with a porous medium, International Journal of Heat and Mass Transfer, 42(6) (1999) 1047-1057.

[53] L. Kumar, B.S. Manjunath, R.J. Patel, S.G. Markandeya, R.G. Agrawal, A. Agrawal, Y. Kashyap, P.S. Sarkar, A. Sinha, K.N. Iyer, S.V. Prabhu, Experimental investigations on melting of lead in a cuboid with constant heat flux boundary condition using thermal neutron radiography, International Journal of Thermal Sciences, 61 (2012) 15-27.

[54] O. Bertrand, B. Binet, H. Combeau, S. Couturier, Y. Delannoy, D. Gobin, M. Lacroix, P. Le Quéré, M. Médale, J. Mencinger, H. Sadat, G. Vieira, Melting driven by natural convection A comparison exercise: first results, International Journal of Thermal Sciences, 38(1) (1999) 5-26.

[55] B. Kamkari, H.J. Amlashi, Numerical simulation and experimental verification of constrained melting of phase change material in inclined rectangular enclosures, International Communications in Heat and Mass Transfer, 88 (2017) 211-219.

[56] X. Xiao, P. Zhang, M. Li, Preparation and thermal characterization of paraffin/metal foam composite phase change material, Applied Energy, 112 (2013) 1357-1366.

[57] P.M. Kamath, C. Balaji, S.P. Venkateshan, Convection heat transfer from aluminium and copper foams in a vertical channel – An experimental study, International Journal of Thermal Sciences, 64 (2013) 1-10.

[58] A. Bhattacharya, V.V. Calmidi, R.L. Mahajan, Thermophysical properties of high porosity metal foams, International Journal of Heat and Mass Transfer, 45(5) (2002) 1017-1031.

[59] E. Assis, L. Katsman, G. Ziskind, R. Letan, Numerical and experimental study of melting in a spherical shell, International Journal of Heat and Mass Transfer, 50(9) (2007) 1790-1804.

[60] M.A. Sheremet, I. Pop, Natural convection in a square porous cavity with sinusoidal temperature distributions on both side walls filled with a nanofluid: Buongiorno's mathematical model, Transport in Porous Media, 105(2) (2014) 411-429.